



Automated crop field extraction from multi-temporal Web Enabled Landsat Data[☆]



L. Yan*, D.P. Roy

Geospatial Science Center of Excellence, South Dakota State University, Brookings, SD 57007, USA

ARTICLE INFO

Article history:

Received 21 June 2013

Received in revised form 4 December 2013

Accepted 9 January 2014

Available online 5 February 2014

Keywords:

Agriculture

Fields

Landsat

Object oriented

WELD

ABSTRACT

An automated computational methodology to extract agricultural crop fields from 30 m Web Enabled Landsat data (WELD) time series is presented. The results for three 150 × 150 km WELD tiles encompassing rectangular, circular (center-pivot irrigation) and irregularly shaped fields in Texas, California and South Dakota are presented and compared to independent United States Department of Agriculture (USDA) National Agricultural Statistics Service (NASS) cropland data layer (CDL) classifications. Coherent fields that are visually apparent were extracted with relatively limited apparent errors of omission or commission compared to the CDL classifications. This is due to several factors. First, the use of multi-temporal Landsat data, as opposed to single Landsat acquisitions, that enables crop rotations and inter-annual variability in the state of the vegetation to be accommodated for and provides more opportunities for cloud-free, non-missing and atmospherically uncontaminated surface observations. Second, the adoption of an object-based approach, namely the variational region-based geometric active contour method that enables robust segmentation with only a small number of parameters and that requires no training data. Third, the use of a watershed algorithm to decompose connected segments belonging to multiple fields into coherent isolated field segments and a geometry-based algorithm to detect and associate parts of circular fields together. A preliminary validation is presented to gain quantitative insights into the field extraction accuracy and to prototype a validation protocol including new geometric measures that quantify the accuracy of individual field objects. Implications and recommendations for future research and large-area applications are discussed.

© 2014 The Authors. Published by Elsevier Inc. All rights reserved.

1. Introduction

The spatial distribution of agricultural fields is a fundamental description of rural landscapes and the location and extent of fields is needed to establish the area of land utilized for agricultural yield prediction, resource allocation, and economic planning (Carfagna & Gallego, 2005; Johnson, 2013; Rudel, Schneider, Uriarte, Turner, Defries, Lawrence, et al., 2009). Since the era of the first Large Area Crop Inventory Experiment (LACIE) the potential for remote sensing in support of agricultural information retrieval has been demonstrated widely (Allen, 1990; Badhwar, 1984; Bauer, Hixson, Davis, & Etheridge, 1978; Becker-Reshef, Justice, Sullivan, Vermote, Tucker, Anyamba, et al., 2010; Jakabauskas, Legates, & Kastens, 2002;

Johnson, 2013; Johnson & Mueller, 2010; MacDonald & Hall, 1980; Ozdogan, 2010; Pitts & Badhwar, 1980; Tucker, Elgin, McMurtrey, & Fan, 1979; Wardlow & Egbert, 2008). With the advent of free Landsat data and improved computing capacity it is now possible to implement processing algorithms that are applicable to continental scale 30 m Landsat data (Roy, Ju, Kline, Scaramuzza, Kovalsky, Hansen, et al., 2010). Identifying agricultural fields from satellite data can be straightforward if undertaken visually by a capable interpreter, for example, by screen digitizing or by interactive thresholding of spectral vegetation indices (Basnyat, McConkey, Meinert, Gatkze, & Noble, 2004; Ferguson, Badhwar, Chhikara, & Pitts, 1986; Lobell, Asner, Ortiz-Monasterio, & Benning, 2003). However, interactive techniques are impractical for large area application and are not amenable to automation. Semi-automated approaches, such as land cover classification, are challenged by factors including within-field spectral variability (caused by spatial variations in soil moisture, salinity, fertility and nutrient limitations, pesticide, herbicide and fertilizer treatment, pollution, pests and diseases) and the temporal variability and spectral similarity between crops and non-crops as a function of their phenological stage, degree of soil background, and the time of satellite observation (Chang, Hansen, Pittman, Carroll, & DiMiceli, 2007; Hall & Badhwar, 1987; Johnson, 2013;

[☆] This is an open-access article distributed under the terms of the Creative Commons Attribution-NonCommercial-ShareAlike License, which permits non-commercial use, distribution, and reproduction in any medium, provided the original author and source are credited.

* Corresponding author at: South Dakota State University Geospatial Science Center of Excellence Brookings, South Dakota 57007, USA. Tel.: +614-886-3172.

E-mail addresses: lin.yan@sdstate.edu (L. Yan), david.roy@sdstate.edu (D.P. Roy).

Rao, 2008). Moreover, they do not extract field objects and to do so requires contextual association of classified pixels to individual fields which is non-trivial. Object-based classification approaches do not operate directly on individual pixels but rather on objects consisting of many pixels that have been grouped together in a meaningful way by image segmentation; when undertaken with geospatial data this is often termed Geographic Object-Based Image Analysis (GEOBIA) (Hay & Castilla, 2008). Commercial software, such as the eCognition package (Definiens, 2009), provide object-based classifiers but they are supervised and require human intervention. A number of automated and semi-automated approaches have been developed to extract objects from satellite data, particularly for high spatial resolution data (Benediktsson, Pesaresi, & Arnason, 2003; Evans, Jones, Svalbe, & Berman, 2002; Huang & Zhang, 2008; Mayer, 2008; Myint, Gober, Brazel, Grossman-Clarke, & Weng, 2011; Shackelford & Davis, 2003), but no automated field extraction methodology applicable to regional or continental scale Landsat data has been developed.

An automated Landsat agricultural crop field extraction methodology is presented. The methodology is object-based, requires no training data, no human interaction, can be parameterized with only a small number of parameters, and is sufficiently computationally efficient and structured to be scalable to continental scale application. Most object-based classifiers purposefully over-segment the scene, typically by applying a multi-scale (hierarchical) iterative segmentation algorithm to generate a set of segmentation solutions (Mason, Corr, Cross, Hoggs, Petrou, Lawrence, et al., 1988; Pavlidis & Liow, 1990; Rydberg & Borgefors, 2001). Rules are then used to group segments to associate them to the same object and to label the objects using image understanding approaches (Shackelford & Davis, 2003; Ton, Sticklen, & Jain, 1991). In this paper the established computer vision based variational region-based geometric active contour segmentation method is used because it requires only a small number of parameters to iteratively generate a segmentation with control over the smoothness of the segment boundaries and segmentation noise (Chan & Vese, 2001). Spatially explicit maps of the probability of crop agriculture and crop field edge presence are derived from Web Enabled Landsat Data (WELD) 30 m time series (Roy et al., 2010) and used as input to the segmentation method. Satellite time series data are used to reduce the impacts of ambiguities due to the phenological stage and the spatial arrangement of field boundaries (irrigation ditches, tracks and roads, fences and hedges, weed and grass swards, trees and shrubs) that in single date satellite images may not be spectrally separable from field interiors (Duveiller & Defourny, 2010; Ozdogan & Woodcock, 2006; Rydberg & Borgefors, 2001). Further, and importantly, time series reduce the influence of missing, shadowed and atmospherically contaminated Landsat observations (Roy, Qin, Kovalskyy, Vermote, Ju, Egorov, et al., 2014; Roy et al., 2010; Zhu & Woodcock, 2012) and enables specific crop and non-crop phenologies to be considered as part of the algorithm implementation. A watershed algorithm is used to decompose connected segments belonging to multiple fields into coherent isolated fields segments. A geometry-based algorithm is used to detect and associate parts of circular fields that are particularly challenging to deal with due to their shape. Results are presented for 150 km × 150 km agricultural regions (each composed of 5000 × 5000 30 m pixels) in Texas, California and South Dakota that encompass rectangular, circular, and irregular fields and a variety of crop types. The results are compared with annual United States Department of Agriculture (USDA) National Agricultural Statistics Service (NASS) cropland data layer classifications (Johnson & Mueller, 2010). A preliminary validation by detailed comparison with field boundaries manually digitized from Landsat 5 Thematic Mapper (TM) data are presented to gain quantitative insights into the field extraction accuracy and to prototype a validation protocol. Implications and recommendations for algorithm refinement and large-area application are discussed.

2. Data and study area

2.1. Landsat data

The methodology requires consistently processed, long-term, geolocated Landsat time series. In this study the weekly Web Enabled Landsat Data (WELD) products were used (Roy et al., 2010). The WELD products enable the development of turnkey approaches to land cover and land cover change characterization (Hansen, Egorov, Potapov, Stehman, Tyukavina, Turubanova, et al., 2014; Hansen, Egorov, Roy, Potapov, Ju, Turubanova, et al., 2011) due to the systematic Landsat processing, including conversion of digital numbers to calibrated top of atmosphere reflectance and brightness temperature, cloud masking, and reprojection into a gridded continental map projection (Roy et al., 2010). Weekly WELD Version 1.5 products were obtained from the USGS EROS (<http://e4ftl01.cr.usgs.gov/WELD/>). The products store for each 30 m pixel location the six reflective top of atmosphere Landsat 7 Enhanced Thematic Mapper Plus (ETM+) bands, the two top of atmosphere thermal bands, bit packed band saturation information, Normalized Difference Vegetation Index (NDVI), two cloud masks, the day of year that the pixel was sensed on, and the number of Landsat observations considered in the week (Roy et al., 2010). The weekly WELD products were generated from all Landsat 7 ETM+ Level 1T data with cloud cover ≤80%. The most recent Landsat calibration knowledge is used in the Level 1T processing to ensure a consistently calibrated Landsat time series with a 5% reflective band calibration uncertainty (Markham & Helder, 2012). The L1T ETM+ geolocation error in the CONUS is less than 30 m even in areas with substantial terrain relief (Lee, Storey, Choate, & Hayes, 2004).

The WELD products are defined in the Albers Equal Area conic projection in separate tiles of 5000 × 5000 30 m pixels referenced using a two digit horizontal and vertical tile coordinate system. Fig. 1 illustrates WELD tile spatial subsets of four weekly WELD products over an agricultural region of Texas. The Landsat 7 ETM+ has a 16 day repeat cycle and each ETM+ L1T scene may be sensed up to 22 or 23 times per year depending on the first January overpass date (Ju & Roy, 2008). The weekly WELD products contain the Landsat 7 ETM+ data sensed in consecutive seven day periods and so at CONUS latitudes they may contain no data, as no Landsat overpassed in that seven day period, or only one Landsat observation. The weekly products have along scan stripes of missing data due to the Landsat 7 ETM+ scan line corrector that failed in 2003 and reduces the usable data in each ETM+ scene by about 22% (Markham, Storey, Williams, & Irons, 2004).

2.2. Independent comparison data

The Cropland Data Layer (CDL) is generated by the United States Department of Agriculture (USDA) National Agricultural Statistics Service (NASS) using Landsat-like resolution satellite imagery and extensive agricultural ground truth via a supervised classification approach (Boryan, Yang, Mueller, & Craig, 2011; Johnson & Mueller, 2010). The CDL defines annually about 110 land cover and crop type classes at 30 m for all the conterminous United States and is used to provide acreage estimates and digital, crop-specific, georeferenced information (Johnson & Mueller, 2010). In this study, the annual CDL for 2008, 2009 and 2010 were obtained from <http://nassgeodata.gmu.edu/CropScape/> and used for qualitative comparison with the field object segmentation results and to provide information on the study area crop types. For 2008, 2009, and 2010 the conterminous United States CDL crop classification accuracy was 76.9%, 80.0%, and 84.3%, respectively (Johnson, 2013). Prior to 2008 the CDL was not available for all the conterminous United States.

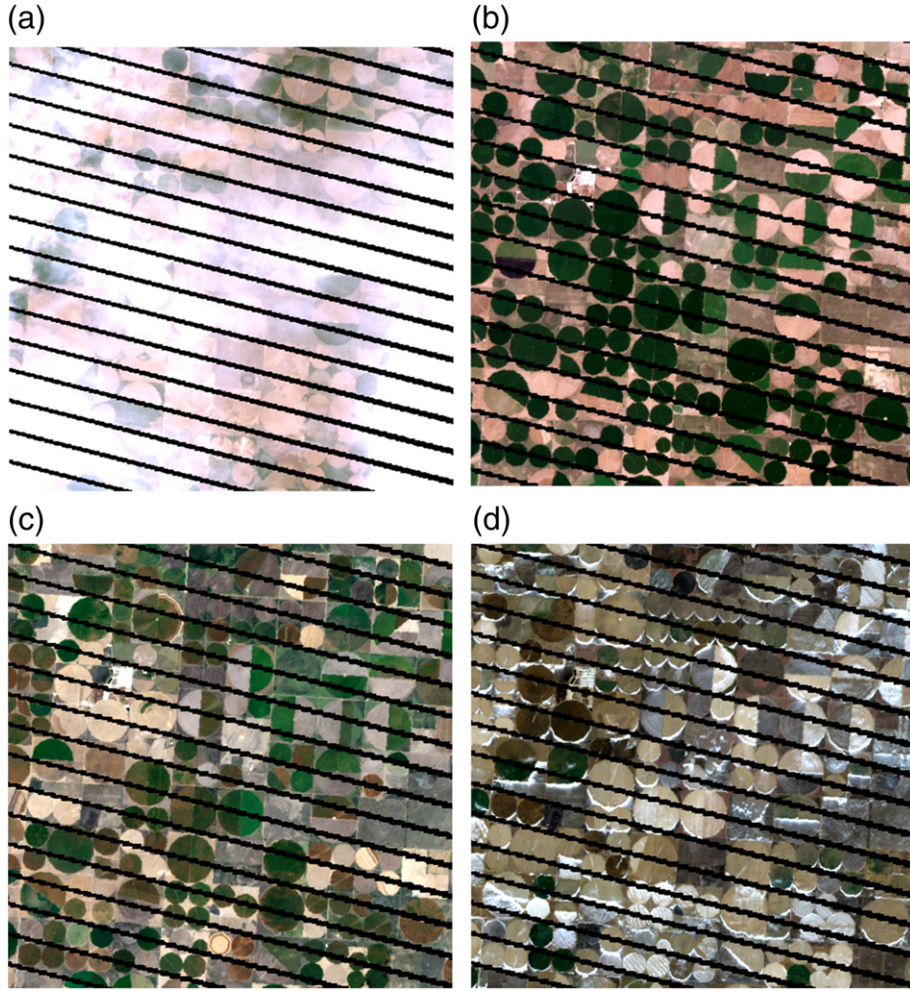


Fig. 1. 500 × 500 30 m pixel subset of WELD tile h13v12 (Northern High Plains, Texas) showing weekly WELD product true color top of atmosphere reflectance for four weeks in 2007, (a): week 13 day 87 (Spring), (b): week 29 day 199 (Summer), (c): week 38 day 263 (Autumn), and (d): week 52 day 359 (Winter).

2.3. Study period and area

Five years of weekly WELD Version 1.5 products were used to accommodate crop rotations and inter-annual variability in the state of the vegetation, to provide more opportunities for cloud-free, non-missing and atmospherically uncontaminated surface Landsat observations of field interiors, boundaries and exteriors, and to enable crop and non-crop phenologies to be considered as part of the implementation. Weekly WELD products from 2006 to 2010 were selected (5 × 52 weeks) as they are the most recently available and overlap temporally with the CDL independent comparison data.

Three WELD tiles, composed of 5000 × 5000 30 m pixels, encompassing 150 × 150 km, located in Texas, California and South Dakota were selected over regions with circular, rectangular and irregularly shaped crop fields, with different crops and crop rotations, including rainfed and irrigated agriculture. The Texas and California tiles were selected because they have extensive, mainly regularly shaped fields that are predominantly irrigated and are surrounded by non-agriculture. The Texas tile was selected as it includes mainly circular fields and the Californian tile was selected as it includes mainly rectangular fields. The South Dakota tile was selected as a more complex test case because it includes extensive but mainly rainfed agriculture, and so typically there is lower spectral contrast with adjacent non-agricultural patches through the growing season, and

because there are irregular field shapes and also considerable within-field variability associated with soil and drainage variations. In addition, the South Dakota tile is located around the authors' university enabling focused ground based crop field extraction assessment. In much of the U.S., a biannual rotation between corn and soybeans is common (Plourde, Pijanowski, & Pekin, 2013), this rotation is prevalent in South Dakota, but multiple crops rotated over several years can also occur which was particularly the case for the Texas and California WELD tiles.

The Texas tile, WELD tile h13v12 (35.22669069° to 36.47820154° North, 101.16169227° to 102.94032758° West), is in the Northern High Plains in the Northern Texas Panhandle. Fig. 1 shows four weekly WELD products over an area of center-pivot irrigation and rectangular roads for a 500 × 500 30 m pixel subset of the Texas tile. The crop and non-crop phenology, the Landsat 7 ETM + scan line corrector stripes, and cloud and snow are clearly evident. This subset is used to illustrate the methodology in detail in Section 3.0. The Texas tile primarily contained CDL classified crops of wheat (56.6% to 65.8% of crop classified pixels for 2008 to 2010), corn (26.8% to 30.3%), cotton (1.8% to 9.9%) and sorghum (4.1% to 6.0%).

The California tile, WELD tile h05v13 (32.58559380° to 33.63728509° North, 113.94813588° to 115.85293402° West), encompasses the southeast corner of California and includes the Imperial Valley. The southern edge is in northern Mexico and the western edge is in Arizona. The tile

contains primarily rectangular fields with CDL classified crops of wheat (25.1% to 40.4% of crop classified for 2008 to 2010), alfalfa or hay (47.3% to 59.2%), and cotton (4.4% to 5.7%).

The South Dakota tile, WELD tile h16v06 (43.37681588° to 44.70557124° North, 96.19343546° to 98.0936587° West), encompasses the cities of Sioux Falls and Brookings in central eastern South Dakota, and parts of western Minnesota and northwestern Iowa. The main CDL classified crops are corn (45.2% to 47.9% of crop classified for 2008 to 2010), soybean (42.2% to 43.2%), wheat (2.4% to 5.3%) and alfalfa or hay (3.5% to 9.9%).

3. Methodology

3.1. Overview

The methodology was applied in the following sequential manner. Spatially explicit 30 m maps of the probability of crop agriculture (Section 3.2) and crop field edge presence (Section 3.3) were derived from the five years of weekly 30 m WELD data and input into a variational region-based geometric active contour (VRGAC) segmentation method to generate candidate crop field segments (Section 3.4). The segmentation uses an iterative approach and the results do not generally over-segment the scene although under-segmentation may occur whereby certain adjacent fields that have indistinct joining boundaries are incorrectly defined as one segment. A watershed algorithm was applied to decompose connected segments belonging to multiple fields into coherent isolated field segments (Section 3.5). A geometry-based algorithm was used to detect and associate parts of circular fields that are particularly challenging to deal with due to their shape (Section 3.6). Finally, a morphological segment cleaning process was applied (Section 3.7).

3.2. Crop probability map generation

A spatially explicit 30 m map defining the probability of crop agriculture was derived from the normalized difference vegetation index (NDVI) stored in the weekly WELD products. The NDVI, derived as the near-infrared minus the red reflectance divided by their sum, is the most widely used vegetation index to study the state and vigor of vegetation (Tucker, 1979). The NDVI has been used to study vegetation phenology (White, de beurs, Didan, Inouye, Richardson, Jensen, et al., 2009) including at Landsat scale (Fisher, Mustard, & Vadeboncoeur, 2006; Kovalsky, Roy, Zhang, & Ju, 2011) and the phenology of agriculture (Jakubauskas et al., 2002; Sakamoto, Wardlow, Gitelson, Verma, Suyker and Arkebauer, 2010; Wardlow & Egbert, 2008). In this study pixels with consistently high seasonal 30 m NDVI values are assumed to be likely to be crop agriculture (Sakamoto et al., 2010). Certain non-agricultural vegetated land cover types may also have this characteristic including forests and grasslands, and this is discussed further in the conclusion.

At each pixel location the 52 weeks of NDVI values were considered and any weekly value labeled as cloudy or saturated in the weekly WELD product were removed. Any gaps in the NDVI time series due to these issues, and missing Landsat due to the acquisition availability and the scan line corrector failure (denoted in the WELD products by a fill value), were filled by linear interpolation of the closest non-missing NDVI values occurring before and after each gap. This was repeated for each of the five years of weekly WELD products. Then for each week (1 to 52) the maximum weekly NDVI from the five years was computed to form a weekly 5-year maximum NDVI time series. The maximum NDVI was used as it preferentially selects vegetated observations with reduced cloud, snow and atmospheric contamination (Holben, 1986; Roy et al., 2010).

Agricultural crops have a pronounced phenology due to crop growth, maturity, and then senescence or harvest (Pan, Li, Zhang, Liang, Zhu and Sulla-Menashe, 2012; Sakamoto et al., 2010). To capture

this phenology a minimum period of d weeks of consistently high NDVI values associated with crop maturity was assumed. The appropriate setting for d can be determined by examination of independent information on the length of the growing season, obviously, in regions with shorter growing seasons a smaller d value is appropriate. In this study, for all three test tiles, d was set to 13 weeks based on examination of the five years of weekly WELD data.

The median NDVI value in each d -week duration window was computed over the weekly 5-year maximum NDVI time series as:

$$\begin{aligned} \text{NDVI}_{(i,j)}^{\text{median}}(\text{week}) &= \text{median}\left\{\text{NDVI}_{(i,j)}(\text{week} + m), m \in \left[-\frac{d}{2}, \frac{d}{2}\right]\right\} \\ \text{NDVI}_{(i,j)}(-\text{week}) &= \text{NDVI}_{(i,j)}(52-w) \end{aligned} \quad (1)$$

where $\text{NDVI}_{(i,j)}^{\text{median}}(\text{week})$ is the median maximum NDVI value computed over a d -week period centered on week , $\text{NDVI}_{(i,j)}(\text{week})$ is the 5-year maximum NDVI value for week , and (i,j) is the pixel location. The median is used as it is robust to outliers and smooths local weekly variations in the 5-year maximum NDVI weekly time series. For each pixel, the maximum of the 52 values of Eq. (1) was derived and the crop probability was computed as:

$$P_{\text{prob}}(i,j) = \begin{cases} 1 & \text{NDVI}_{(i,j)}^{\text{max}} \geq \text{NDVI}_{0.95} \\ \frac{\text{NDVI}_{(i,j)}^{\text{max}}}{\text{NDVI}_{0.95}} & \text{NDVI}_{(i,j)}^{\text{max}} < \text{NDVI}_{0.95} \end{cases} \quad (2)$$

where $P_{\text{prob}}(i,j)$ is the crop probability at pixel location (i,j) , $\text{NDVI}_{(i,j)}^{\text{max}}$ is the maximum annual median NDVI value (i.e. maximum of Eq. (1) over 52 weeks), and $\text{NDVI}_{0.95}$ is the 95th percentile value of all the $\text{NDVI}_{(i,j)}^{\text{max}}$ values in the WELD tile. The 95th percentile is used to avoid the influence of outliers. Fig. 2 shows an example for the Texas subset illustrated in Fig. 1. The circular center-pivot irrigation fields are evident and the stripes due to the Landsat ETM+ scan line corrector problems seen in Fig. 1 are only slightly apparent because of the use of five years of data and the smoothing provided by Eq. (1). Within some of the circular fields, "pie slice" circular sectors with lower crop probability are evident

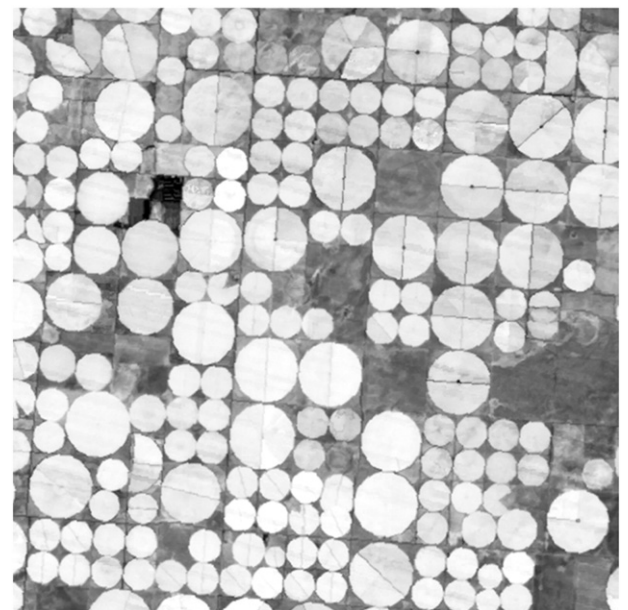


Fig. 2. Crop probability map for the 500×500 30 m Texas spatial subset illustrated in Fig. 1, derived by Eqs. (1) and (2) from 5-years of weekly WELD products (2006 to 2010) and assuming a $d = 13$ week value.

and are associated primarily with temporal variations in the agricultural cover over the five years of WELD data.

3.3. Crop field edge probability map generation

A spatially explicit 30 m map defining the probability of crop field edge presence was extracted from the weekly WELD reflectance data. For each pixel in each weekly WELD product, the spectral distance with its neighboring pixels was computed as:

$$d_{\text{week}, k}^{\rho}(i, j) = \sqrt{\sum_{\lambda \in \{2,3,4,5,7\}} (\rho_{\text{week}, \lambda}(i, j) - \rho_{\text{week}, \lambda}(i+x(k), j+y(k)))^2} \quad (3)$$

$x(k=1 \dots 8) = \{0, -1, -1, -1, 0, 1, 1, 1\}$
 $y(k=1 \dots 8) = \{1, 1, 0, -1, -1, -1, 0, 1\}$

where $d_{\text{week}, k}^{\rho}(i, j)$ is a measure of the spectral distance of a pixel located in the weekly WELD product for a given week at pixel location (i, j) with respect to pixel k located in any of up to eight adjacent pixels with reflectance data defined by offsets $x(k), y(k)$. If there were no reflectance data at (i, j) or no adjacent pixels with reflectance data, denoted by a fill value in the weekly WELD products, then Eq. (3) was not defined. The spectral distance was computed with respect to the Landsat ETM + reflective wavelength bands 2 (green, 0.53–0.61 μm), 3 (red: 0.63–0.69 μm), 4 (near-infrared: 0.78–0.90 μm), 5 (middle: 1.55–1.75 μm) and 7 (middle-infrared: 2.09–2.35 μm). The shortest wavelength Landsat ETM + (band 1, 0.45–0.52 μm) was not used because it is the most sensitive Landsat ETM + band to atmospheric scattering (Ju, Roy, Vermote, Masek, & Kovalskyy, 2012; Roy et al., 2014) and was found to add more noise than information when included in Eq. (3). Similarly, the two thermal wavelength Landsat ETM + bands were not used as they have a 60 m native resolution and their inclusion smoothed the results generated using just the 30 m reflective wavelength bands.

The spectral distance (Eq. (3)) enhances edges of all kinds including non-agricultural ones. As for the crop probability map generation, the NDVI was used to emphasize agriculture. An NDVI distance was calculated as:

$$d_{\text{week}, k}^{\text{NDVI}}(i, j) = |\text{NDVI}_{\text{week}}(i, j) - \text{NDVI}_{\text{week}}(i+x(k), j+y(k))| \quad (4)$$

$x(k=1 \dots 8) = \{0, -1, -1, -1, 0, 1, 1, 1\}$
 $y(k=1 \dots 8) = \{1, 1, 0, -1, -1, -1, 0, 1\}$

where $d_{\text{week}, k}^{\text{NDVI}}(i, j)$ is a measure of the NDVI distance of a pixel located in the weekly WELD product for a given week at pixel location (i, j) with respect to pixel k located in any of eight adjacent pixels defined by offsets $x(k), y(k)$. If there were no NDVI data at (i, j) , or no adjacent pixels with NDVI data, then Eq. (4) was not defined. Fields typically have more homogenous NDVI than their boundaries and so $d_{\text{week}, k}^{\text{NDVI}}(i, j)$ is usually reduced in field interiors.

An estimate of the crop field edge presence for each week was defined as the product of the NDVI at each pixel location and the spectral and NDVI distances weighted by the spatial proximity (diagonal, vertical or horizontal) of the pixel neighbors as:

$$e_{\text{week}}(i, j) = \text{NDVI}_{\text{week}}(i, j) \cdot \frac{\sum_{k=1}^8 d_{\text{week}, k}^{\rho}(i, j) \cdot w_k}{\sum_{k=1}^8 w_k} \cdot \frac{\sum_{k=1}^8 d_{\text{week}, k}^{\text{NDVI}}(i, j) \cdot w_k}{\sum_{k=1}^8 w_k} \quad (5)$$

$w(k=1 \dots 8) = \{1, \sqrt{2}/2, 1, \sqrt{2}/2, 1, \sqrt{2}/2, 1, \sqrt{2}/2\}$

where $e_{\text{week}}(i, j)$ provides an estimate of the agricultural field edge presence for a given week at pixel location (i, j) , $\text{NDVI}_{\text{week}}(i, j)$ ensures that pixels with higher NDVI have higher edge presence probability,

and $d_{\text{week}, k}^{\rho}(i, j)$ and $d_{\text{week}, k}^{\text{NDVI}}(i, j)$ are defined by Eqs. (4) and (5), respectively.

The crop field edge probability was computed as:

$$P_{\text{edge}}(i, j) = \frac{\sum_{\text{week}=1}^n e_{\text{week}}(i, j)}{n} \quad (6)$$

where $P_{\text{edge}}(i, j)$ is the field edge presence probability, $e_{\text{week}}(i, j)$ is defined by Eq. (5), and n is the number of weeks at pixel location (i, j) over the five years with non-missing $e_{\text{week}}(i, j)$ values. Fig. 3 shows an example for the Texas subset illustrated in Fig. 1. The circular center-pivot irrigation fields are visually evident and the boundaries of crops within the fields that changed within and between years seen by the different radii locations and different radii edge intensities.

3.4. Candidate agriculture field extraction

The crop probability map (Eq. (2)) and the crop field edge presence probability map (Eq. (6)) were input into a segmentation method to generate a candidate binary field segmentation map. The established variational region-based geometric active contour (VRGAC) method was used because it requires only a small number of parameters to iteratively generate a segmentation with control over the smoothness of the segment boundaries and segmentation noise (Chan & Vese, 2001). It uses a level set function approach that enables numerical computations on a fixed Cartesian grid without having to parameterize segment curve and surface properties that can be particularly complex to parameterize, especially for segments that change topology, for example, if they split into parts or develop holes (Osher & Sethian, 1988). The level set function is a two dimensional matrix with each element corresponding to a pixel location and with values storing the spatial distance to the closest segment boundary. Signed distances are stored so that locations inside a segment (termed the foreground) are negative and increase in value for locations closer to the segment boundary, and locations outside of the segment (termed the background) have positive values. Fig. 4 shows an example field segmentation and the equivalent level set function. The level set function was derived in a computationally efficient manner using an implementation of the Chamfer 3–4 distance transform (Butt & Maragos, 1998).

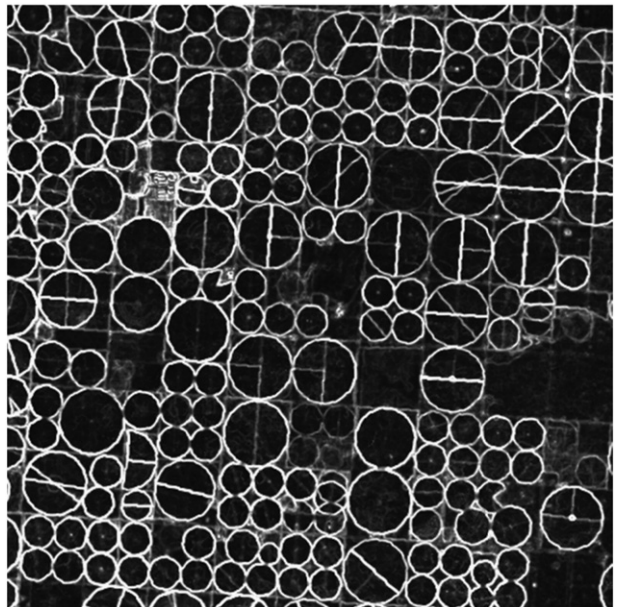


Fig. 3. Crop field edge presence probability map for the 500 × 500 30 m Texas spatial subset illustrated in Fig. 1, derived by Eq. (6) from 5-years of weekly WELD products (2006 to 2010).

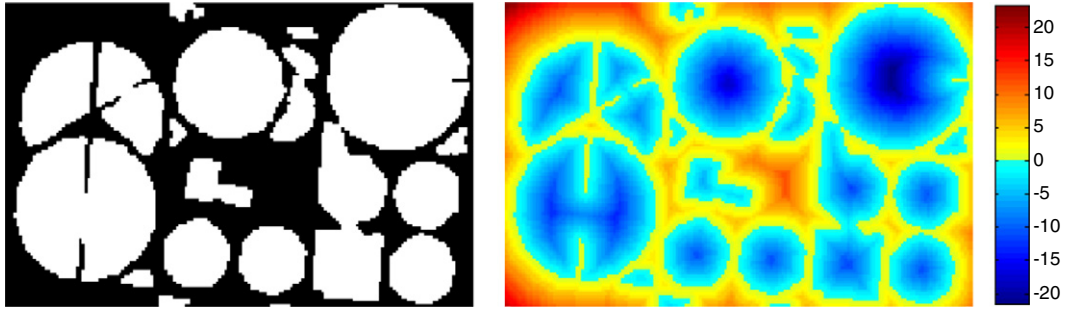


Fig. 4. left: Example 164 × 107 30 m pixel segmentation into fields (white) and non-fields (black); right: corresponding level set function where each pixel location stores the signed distance (in units of pixel dimensions) to the closest segment boundary, the negative distances occur within the segments (shown in blue shades) and the positive distances occur outside segments (shown in yellow to red shades).

An initial binary segmentation was computed in order to subsequently derive an initial level set function. The initial binary segmentation was derived as:

$$s(i, j) = \begin{cases} 1 & P_{\text{prob.}}(i, j) \geq 0.85 \\ 0 & P_{\text{prob.}}(i, j) < 0.85 \end{cases} \quad (7)$$

where $s(i, j)$ is the initial segmentation and $P_{\text{prob.}}(i, j)$ is the agricultural crop probability. A probability threshold of 0.85 provided a reasonable initial binary segmentation into fields although the final results were not sensitive to setting this probability threshold over the range 0.5 to 0.9.

The VRGAC method was applied to update the level set function in an iterative manner (Chan & Vese, 2001) as:

$$\phi(i, j)_{n+1} = \phi(i, j)_n + \delta_\varepsilon(\phi(i, j)_n) \left(-\lambda_1 \cdot P_{\text{prob.}}(i, j) + \mu \cdot \kappa(i, j) \right) + \lambda_2 \cdot P_{\text{edge}}(i, j) \quad (8)$$

where $\phi(i, j)$ is the level set function composed of signed distances at each pixel location (i, j) , $\phi(i, j)_{n+1}$ is the updated version of $\phi(i, j)_n$, $P_{\text{prob.}}(i, j)$ is the crop probability (Eq. (2)), $P_{\text{edge}}(i, j)$ is the crop field edge presence probability (Eq. (6)), $\kappa(i, j)$ is the level set curvature map defined by Eq. (9), δ_ε is an approximated Delta function defined by Eq. (10), and λ_1 , λ_2 and μ are scalar constants that control the segmentation performance. On the first iteration, $\phi(i, j)_n$ is defined by the level set function of the initial segmentation (Eq. (7)). Note that the values in $P_{\text{prob.}}(i, j)$ and $P_{\text{edge}}(i, j)$ never change from what was computed by Eqs. (2) and (6).

The curvature map $\kappa(i, j)$ is defined (Caselles, Catte, Coll, & Dibos, 1993) as:

$$\kappa(i, j) = \frac{\phi_i^2(i, j)\phi_{jj}''(i, j) - 2\phi_i'(i, j)\phi_j'(i, j)\phi_{jj}''(i, j) + \phi_j^2(i, j)\phi_{ii}''(i, j)}{\left(\phi_i^2(i, j) + \phi_j^2(i, j)\right)^{\frac{3}{2}}} \quad (9)$$

where

$$\phi_i'(i, j) = \frac{\phi(i+1, j)_n - \phi(i-1, j)_n}{2}$$

$$\phi_j'(i, j) = \frac{\phi(i, j+1)_n - \phi(i, j-1)_n}{2}$$

$$\phi_{ii}''(i, j) = \phi(i+1, j)_n - 2\phi(i, j)_n + \phi(i-1, j)_n$$

$$\phi_{jj}''(i, j) = \phi(i, j+1)_n - 2\phi(i, j)_n + \phi(i, j-1)_n$$

$$\phi_{ij}''(i, j) = \frac{\phi(i+1, j+1)_n + \phi(i-1, j-1)_n - \phi(i+1, j-1)_n - \phi(i-1, j+1)_n}{4}$$

The Delta function (δ_ε) is defined to constrain each update of the level set function to be applied to an area within a narrow band of width ε pixels as:

$$\delta_\varepsilon(x) = \begin{cases} 1, & \text{if } x = 0 \\ 0, & \text{if } |x| > \varepsilon \\ \frac{1}{2\varepsilon} \left[1 + \cos\left(\frac{\pi x}{\varepsilon}\right) \right], & \text{otherwise} \end{cases} \quad (10)$$

In Eq. (10) ε is set usually to between one and two pixels (Lankton & Tannenbaum, 2008) and in this study it was set to 1.5 pixels.

For each iteration (Eq. (8)) the new level set function ($\phi(i, j)_{n+1}$) can have pixel locations with changed sign relative to the previous iteration function values ($\phi(i, j)_n$). Thus, pixels can be pushed from the foreground to background, or from the background to the foreground, after each iteration. The iteration is stopped when a pre-defined stable state is reached, for this study, when the accumulated number of pixels with sign changes in 20 consecutive iterations corresponded to less than 0.001% of the total number of pixels in the WELD tile. The output candidate binary field segmentation is defined by the positive values (i.e. foreground pixels in $\phi(i, j)_{n+1}$) and each unique segment is composed of spatially adjacent neighboring foreground pixels. The output candidate binary crop field segmentation can be quite different to the initial segmentation (Eq. (7)).

The segmentation performance is controlled by the scalar parameters λ_1 , λ_2 and μ in Eq. (8) (Caselles et al., 1993; Chan & Vese, 2001; Malladi, Sethian, & Vemuri, 1995). The terms $\lambda_1 \cdot P_{\text{prob.}}(i, j)$ and $\lambda_2 \cdot P_{\text{edge}}(i, j)$ generate forces that attempt to keep the pixels in the foreground and background, respectively. The curvature term $\mu \cdot \kappa$ smoothes the segment boundaries and suppresses noisy segments according to the segment boundary curvature. In this study the VRGAC was run twice. First it was run on the initial segmentation (Eq. (7)) with $\lambda_1 = 0.01$, $\mu = 0.01$, $\lambda_2 = 3$ in an attempt to trim the segment boundaries according to the edge probability and thus to enhance the separation of foreground segments between each other and from the background. The results of the first run were then used as input to the VRGAC method that was run again with $\lambda_1 = 0.01$, $\mu = 1$, and $\lambda_2 = 0.01$ in an attempt to smooth the segment boundaries and reduce noise. By running the VRGAC method twice the sensitivity of the candidate binary crop field segmentation to the exact settings of λ_1 , λ_2 and μ was reduced. Fig. 5 shows the resulting candidate field extraction for the example Texas subset.

3.5. Crop field object morphological decomposition

The candidate crop field extraction may be imperfect with certain adjacent fields incorrectly defined as one segment. Examples are evident in Fig. 5. This occurs if the boundary between adjacent joining crop fields is indistinct, for example, if the boundary is smaller than the 30 m Landsat pixel resolution, or occurs near the middle of a 30 m pixel. In particular, it may occur when a curved boundary meets the curved or straight

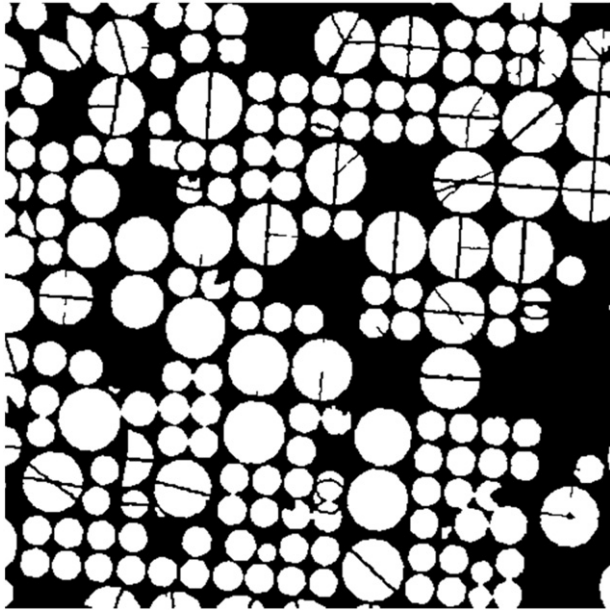


Fig. 5. Variational region-based geometric active contour segmentation results derived by application of Eq. (8) to the 500 × 500 30 m Texas spatial subset results illustrated in Figs. 2 and 3 (see text for details).

boundary of an adjacent field. In addition, sub-pixel Landsat geolocation errors will smooth the field boundary representation in $P_{\text{edge}}(i, j)$ and shift or broaden the vegetated boundary in $P_{\text{prob}}(i, j)$ due to the interaction of geolocation errors and the maximum NDVI compositing used to derive $P_{\text{prob}}(i, j)$ (Roy, 2000).

A morphological decomposition algorithm was implemented to decompose the connected segments belonging to multiple fields into isolated fields. The algorithm is based on a watershed method developed originally for application to digital elevation data to derive hydrological watersheds i.e. the land area where all rainfall goes to the same place (Bleau & Leon, 2000). It first finds regional minima in the level set function (i.e., the regionally most negative signed distance value locations). The gradients (first derivatives in the pixel x, y and two diagonal directions) of the signed distances are derived for each pixel. A region growing algorithm starting from each minimum location is applied to the gradients and those pixels where the gradient sign changes are used

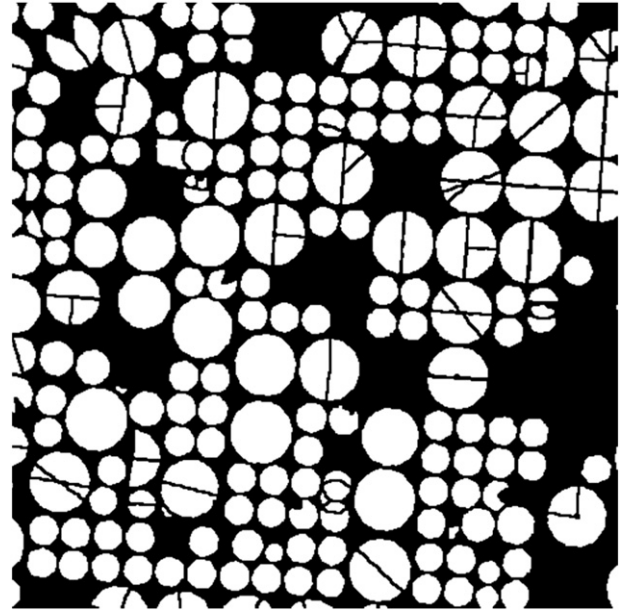


Fig. 7. Results of the crop field object morphological decomposition of the candidate field segments illustrated in Fig. 5 (500 × 500 30 m Texas spatial subset).

to define the watershed boundaries (Bleau & Leon, 2000). The watershed algorithm typically creates too many watersheds if the minima are in close proximity. To solve for this problem, candidate field segments with level set functions containing more than one minima were tested using the following topological skeleton algorithm. The topological skeleton, also referred to as the medial axis, of an object is the set of all points having more than one closest point on the object's boundary (Lee, 1982). Fig. 6 illustrates the level set function, the topological skeleton, and the detected minima, for two segments. The minima by definition lie on the skeleton. Let $\text{Skeleton}(m_1, m_2)$ denote the union of the pixels in the skeleton connecting two minima m_1 and m_2 . Each pair of minima were considered as one if:

$$\left\{ \begin{array}{l} \text{no other minima occur in } \text{Skeleton}(m_1, m_2) \\ \min |\phi(\text{Skeleton}(m_1, m_2))| \geq \frac{2}{3} \min(|\phi(m_1)|, |\phi(m_2)|) \end{array} \right. \quad (11)$$

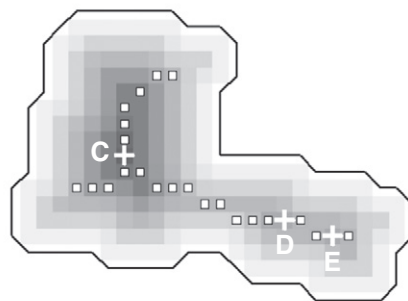
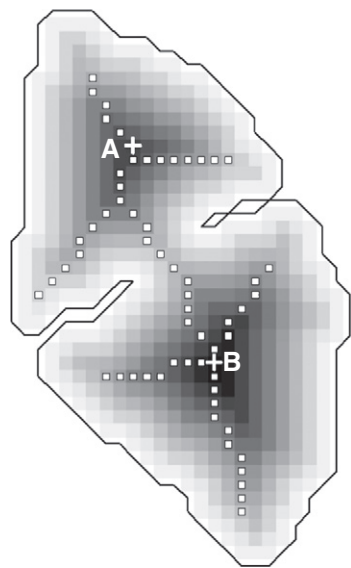


Fig. 6. Example illustrative level set functions for two segments. The regional minima of the level set functions (i.e., the most negative signed distance value locations) are shown by crosses. The topological skeletons are illustrated by white squares. The black outlines are shown for illustrative clarity only.

The latter minimization test typically finds “bottleneck” locations where the signed distance values are low because of their close proximity to a boundary on two sides. In this way the two minima (A, B) illustrated in Fig. 6 are *not* considered as one and the watershed algorithm will split the segment, whereas the three minima (C, D, E) are considered as one so the segment is not split.

Fig. 7 shows the results of applying the splitting approach to the candidate field segments illustrated in Fig. 5. These detailed results indicate that the algorithm appears to work well for these data.

3.6. Circular-sector segment detection and circular field association

Center-pivot irrigation systems use a pipe on wheels pivoting around a central point to water crops via sprinklers. Their fields are perfectly circular and describe a proportion of a circle corresponding to the degree of rotation of the sprinkler around the central pivot. As noted with respect to Figs. 2 and 3, “pie slice” circular sectors may be evident within some circular fields. This is due to crop rotation within the fields and sometimes due to the presence of access roads to the central pivot. These different cases may result in circular sectors that belong to the same central pivot being labeled as separate segments. This is evident in the segmentation results illustrated in Fig. 7.

A geometry-based algorithm was developed to detect parts of circular fields that share the same central pivot and then associate them together. There are a number of circle detection algorithms adapted for different degrees of ellipticity and data type, mostly based on Hough transformations (Davies, 1987; Ioannou, Huda, & Laine, 1999; Smereka & Dulęba, 2008) or geometric analysis of boundary shape (Honkanen, Saarenrinne, Stoor, & Niinimaki, 2005; Pla, 1996). In this application, circular field objects may be segmented into different pieces which degrades the applicability of Hough transformation circle detection and boundary shape based methods. Furthermore, the edges of the circular fields may not be smooth or regular which can degrade the efficacy of boundary shape based methods. Consequently, in this study an empirical divide and conquer approach based on shape fitting was used to detect circular sector segments with arbitrary parameters (circle center location, radius and degree of the central angle) and to associate sectors that belong to the same circle.

Circular sectors were detected in an initial “divide” step. Analysis of the circular sectors in the California and Texas test WELD tiles, that include many pivot irrigation fields, indicated that a circle center was typically no more than three pixels away from the closest edge of any circular sector segment. This three pixel gap occurs primarily due to the variational region-based geometric active contour segmentation parameterization and is evident in Fig. 5. Also gaps may occur when the apex of the circular sector is smaller than a 30 m pixel dimension and because crops may not be planted or irrigated near the central pivot. Consequently, the boundary of each segment was morphologically dilated (Serra, 1988) by three pixels to provide a locus of potential circle center locations along the dilated boundary. From each potential circle center pixel location, rays of a specified length were cast outwards in every direction and the number of pixels along each ray falling within the segment counted. For the rays with one or more pixels falling within the segment, the following fitting statistic was computed:

$$\text{fit}(i, j, l) = \frac{\sum_{r=1}^k n_r^o + \sum_{r=1}^k n_r^c}{\sum_{r=1}^k n_r + \sum_{r=1}^k n_r^o} \quad (12)$$

where $\text{fit}(i, j, l)$ is a fitting statistic for the k rays with length l pixels starting at potential circle center pixel location (i, j) , n_r is the number (≥ 1) of pixels along ray r that fall within the segment, n_r^o is the number of pixels (≥ 0) along ray r that are not in the segment (considered an omission error), and n_r^c is the number of pixels (≥ 0) that occur within

the segment on a straight line from the end of the ray to the segment boundary furthest from (i, j) (considered a commission error).

To compute Eq. (12) the ray length (l) was varied systematically from 10 to 30 pixels (i.e., from 300 m to 900 m set according to the radii lengths of the circular agriculture fields observed in the two WELD test tiles), and for each potential circle center pixel location (i, j) , the minimum of Eq. (12) was derived. If at any potential circle center pixel location (i, j) the minimum of Eq. (12) was less than 0.27, then the segment was classified as a circular sector and the location and the radius length were recorded. The 0.27 threshold was found by exhaustive application of this method and examination of all the segments in the California and Texas test WELD tiles; less than 5% of circular sectors

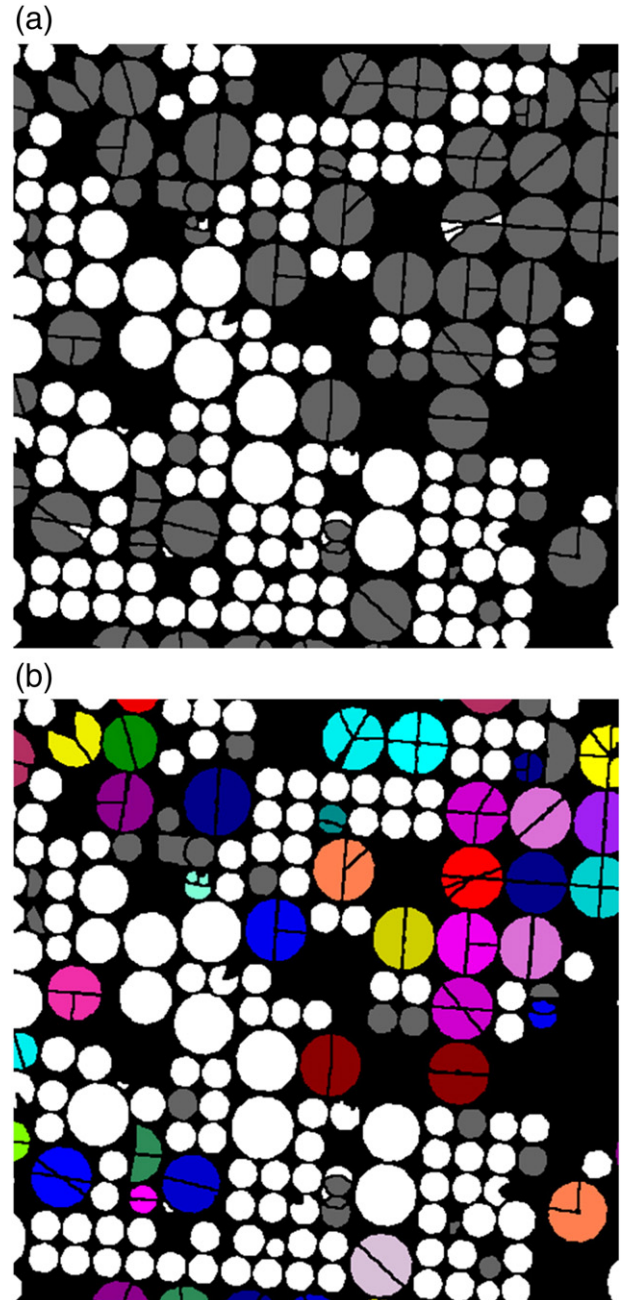


Fig. 8. (a) Initial “divide” step detected circular sector segments (gray); (b) Subsequent “conquer” step segments, the non-gray and non-white colors show refined circular sectors that are labeled as belonging to the same circular field. Results shown for the candidate crop field segments illustrated in Fig. 7 (500 × 500 30 m Texas spatial subset).

provided a minimum of Eq. (12) greater than 0.27, and the greater majority were detected with a threshold of 0.19 or smaller.

The detected circular sectors from the initial “divide” step are illustrated in Fig. 8(a) (shaded gray) for the Texas subset. Several of the small circular fields and a segment (top left of figure) that is square with only one curved side were detected incorrectly as circular sectors. This occurs because these segments are small and compact, but this is unimportant if they are not subsequently associated together. Some of the circular sectors missed by the initial “divide” step are also evident in Fig. 8(a) and they typically have small central angles (<45°).

The circular sectors detected in the initial “divide” step were examined in a subsequent “conquer” step to identify those that belong to the same central pivot, i.e., that belong to the same circular field, so that they could be associated together. The first test in the “conquer” step is illustrated in Fig. 9 that shows six segments and the potential circle center pixel locations (gray pixels) for the five segments (A, B, C, D, E) that were detected as circular sectors by the “divide” step. The segments with potential circle center pixel locations no more than four pixels apart were assumed to be likely to belong to the same circular field. This simple association rule is quite powerful. For example, in Fig. 9, segments A and B are labeled as belonging to the same circular field, and segments C, D and E as belonging to another circular field. If a segment detected as a circular sector has more than one potential circle center pixel location (such as segment C), then only the location with other potential circle centers in its four pixel proximity is considered.

To prevent incorrect association of circular sectors to the same circular field, which may occur for small closely adjacent circular sectors that have close potential circle center pixel locations, an additional step was implemented. For each set of associated circular sectors the potential circle center pixel locations (i, j) and the corresponding radius lengths (l) that the sectors were detected/associated with were considered. The range of the radius lengths and the coordinates (bounding box) of the potential circle center pixel locations were derived. The initial “divide” step was repeated but considering the union of the associated circular sectors and new potential circle center pixel locations at every location within the bounding box with ray lengths varied over the range of the derived radius lengths. If the minimum of Eq. (12) for the union of the associated circular sectors was smaller or equal to 0.19 then the association was accepted. The circular field center and radius was then defined by the i, j , and l values of the ray that provided the minimum of Eq. (12).

A final step was implemented to identify missing circular sectors that were not detected by the above steps, such as, for example, segment F in Fig. 9. Segments not detected as circular sectors but that occurred within the radius (l) of each associated circular sector field center were identified. For these segments the following metrics were computed. First the ratio of the length of the one or more segment sides that occurred within three pixels of an adjacent circular sector to the length of the segment perimeter (in pixels) was computed. If the ratio was greater than $1/(2 + \pi/2)$, i.e., the ratio of the radius to the perimeter of a 45° circular sector (length of two straight edges and a quarter circle curve), then the missing segment was determined to be part of the circular field. However, as missing segments can fall partially or completely within the field radius (l), the degree of segment commission was quantified by casting rays from the field center (i, j) and computing for the rays with one or more pixels falling within the segment the following fitting statistic:

$$fit = \sum_{r=1}^k n_r^c / \left(\sum_{r=1}^k n_r + \sum_{r=1}^k n_r^o \right) \quad (13)$$

where fit is the fitting statistic for the k rays with fixed length equal to the field radius starting at the field center, n_r , n_r^o and n_r^c are defined as for Eq. (12). If the segment had a value of Eq. (13) greater than 0.1 then more than 10% of it falls outside of the field radius and so it was rejected as belonging to the circular field.

The results of the above “conquer” step are shown in Fig. 8(b). The greater majority of the circular fields composed of two or more circular sectors are associated correctly (shown by different colors). Only two small adjacent circular fields each composed of two circular segments with unusually curved interior radii (shown middle bottom of Fig. 8b) are not associated. However, inspection of the 2007 WELD weekly data (Fig. 1) and the crop field edge presence probability map generated from the five years of weekly WELD data (Fig. 3) indicates that in 2007 there were initially two circular fields but that in a subsequent year the farmer moved or placed a new irrigation pivot midway between the two fields so that over the five years the footprints of three fields were superimposed. Evidently, if field boundaries are physically moved during the period of the satellite time series acquisition, then fields are less easily extracted. This is a fundamental change detection issue.

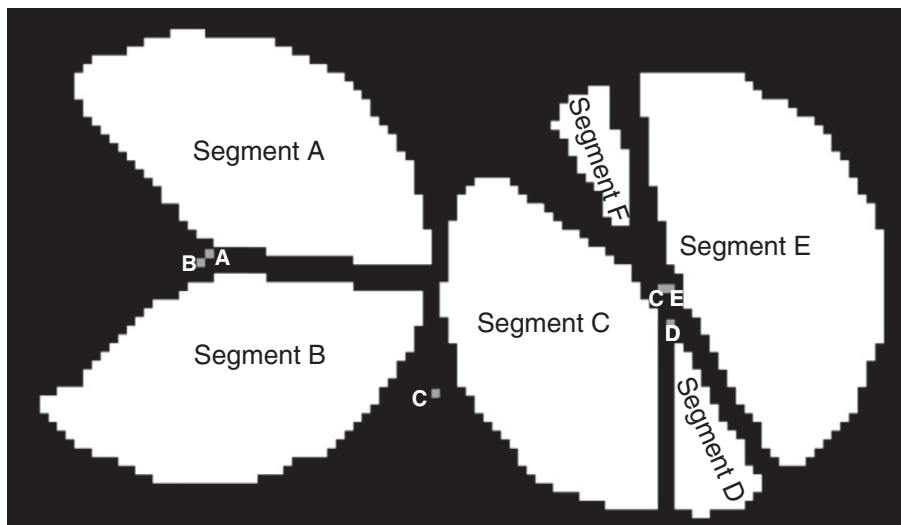


Fig. 9. Example association of circular sector segments to the same circular field. Segments A, B, C, D and E are detected as circular sector segments and their corresponding potential circle center pixel locations are illustrated (gray pixels). Segment C has two potential circle center pixel locations. In this example, segment F is not detected as a circular sector by the initial “divide” step of the detection algorithm.

3.7. Final segmentation cleaning

The resulting segmentation was refined by application of a two-pixel dilation and then a one-pixel erosion morphological filter (Serra, 1988) that cleans indented field edges. Importantly this morphological filtering is applied to each segment independently and so adjacent fields are not connected together. The morphological filtering artificially expands small isolated fields composed of only a few pixels; for this reason, and because of the geometric filtering, fields composed of less than 16 Landsat pixels are considered conservatively to be extracted unreliably.

The results of the final segmentation cleaning are illustrated in Fig. 10, and when compared to the original input data (Fig. 1) illustrate qualitatively that the methodology works successfully in that it produces coherent associations that are visually apparent to a human interpreter.

4. Illustrative results

4.1. Texas

Fig. 11 shows the crop field extraction results for the 150×150 km Texas WELD tile. The colors denote the different field segment labels and black shows locations where no fields were extracted. The results capture the extensive number of circular center-pivot irrigation fields in the north of the tile encompassing the cities of Dalhart, Stratford and Dumas. The north of the tile is predominantly irrigated agriculture whereas the center is covered predominantly by dry grass and shrub lands. This is clearly evident in Figs. 12 and 13 that show the crop and field edge probability maps generated from the five years of weekly WELD products, respectively. The crop field edge probability map captures not only field edges but also the edges of water bodies and roads that were adjacent to vegetation which suggests that the methodology could be adapted to detect these feature types. The central dry grass and shrub area has low probabilities compared to the regions with detected fields to the north and south. In Fig. 11 there is an evident large incorrectly labeled field in the central eastern part of the tile

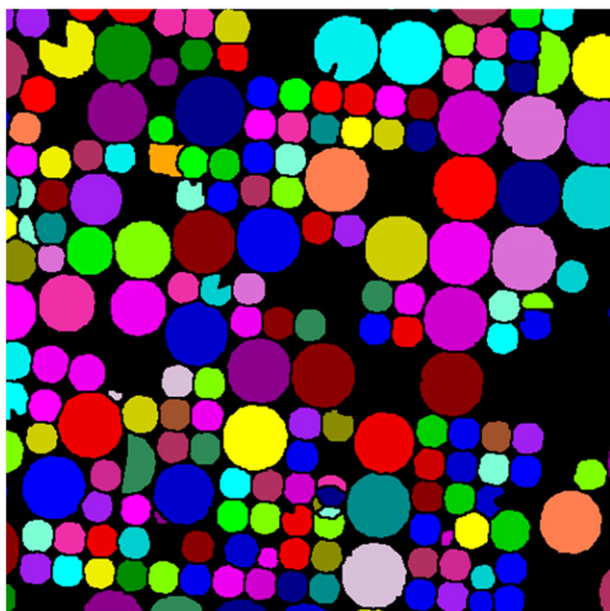


Fig. 10. Final crop field extraction results after segment cleaning. The colors denote different field segment labels.

(colored green, area 2.27 km^2) that was classified as “Open Water” in the 2008 Crop Data Layer (CDL) and as “Woody Wetlands” in the 2009 and 2010 CDL products. Closer inspection reveals that this is a region of ephemeral wetlands on the western side of Lake Meredith.

Fig. 14 shows a histogram of the field areas extracted from the Texas WELD tile. Each field area was calculated by counting the number of pixels in each unique field segment and then multiplying by the area of a $30 \times 30 \text{ m}$ pixel (0.0009 km^2). A total of 6556 fields were extracted with a median area of 0.4743 km^2 and ranging from 0.0027 km^2 to 2.651 km^2 . The histogram is binned with an area equivalent to 16 Landsat pixels (0.0144 km^2) and so the first histogram bin shows how many fields were too small to be extracted reliably, corresponding to about 0.5% of the total number of extracted fields. The histogram exhibits three peaks at 0.067 km^2 , 0.485 km^2 and 1.968 km^2 . The 0.485 km^2 and 1.968 km^2 peaks correspond to the areas of the two sizes of circular center-pivot irrigation fields that are particularly evident in Fig. 10. These areas indicate center-pivot systems with water pipe lengths of about 390 m and almost exactly twice as long at 790 m. These dimensions correspond to 0.24 miles and 0.49 miles, i.e. the radii required to irrigate quarter section fields (0.5×0.5 mile) and full section fields (1×1 mile) that were originally surveyed in much of the western United States (Pitts & Badhwar, 1980).

A detailed 21×27 km Texas subset and the corresponding CDL for 2008, 2009 and 2010 are illustrated in Fig. 15. The subset CDL data includes 19 crops and are illustrated using the color legends provided by the USDA NASS (<http://www.nass.usda.gov/research/Cropland/sarsfaqs2.html>). Of these 19 crop types only six were classified for more than 0.5% of the subset pixels over the three years. The evident classification noise in each CDL product precludes an unambiguous field boundary delineation for many of the fields. The CDL classification noise is due to factors including the supervised classification sensitivity to within-field spectral variability, the input satellite data quality and pre-processing, and the use of insufficiently representative training data for the large number of sometimes spectrally similar crops (Boryan et al., 2011; Johnson & Mueller, 2010). Although the CDL is a per-pixel supervised classification, not a field object map, visual comparison does indicate a visual correspondence between the CDL data and the extracted field results. The three years of CDL data indicate complex crop rotations including rotations within pivot irrigation fields that underscore the need for the circular-sector segment detection and circular field association. There are a minority of small and irregular extracted fields that show no clear correspondence with the annual CDL data and, although they may be ascribed to agriculture in 2006 and 2007, it is unclear if they are irregular fields or commission errors. Farmers may plant crops in the corners of the square or rectangular areas that are not pivot irrigated but these are not evident in the CDL data.

4.2. California

Fig. 16 shows the crop field extraction results for the 150×150 km California WELD tile and Fig. 17 shows the crop probability map generated from the five years of weekly WELD products (the crop field edge probability map is not shown to save space). The tile is predominantly desert although the southern end of the saline lake, the Salton Sea, lies in the north west corner. This region, despite desert conditions, has extensive agriculture due to irrigation from the Colorado River whose floodplain is evident in the crop probability map (Fig. 17) meandering south from the north east to the central south tile edge. Three regions of fields were extracted, and within each region coherent islands of no fields were detected corresponding to urban areas – in the west to the cities of Calipatria, Brawley and El Centro, in the southwest to the Mexican city of Mexicali, in the southeast to Yuma, and in the northeast to Blythe. These cities and the road network between fields are also clearly evident by their low crop probability in Fig. 17. At the scale illustrated in Fig. 16 one obvious commission error is apparent, the large

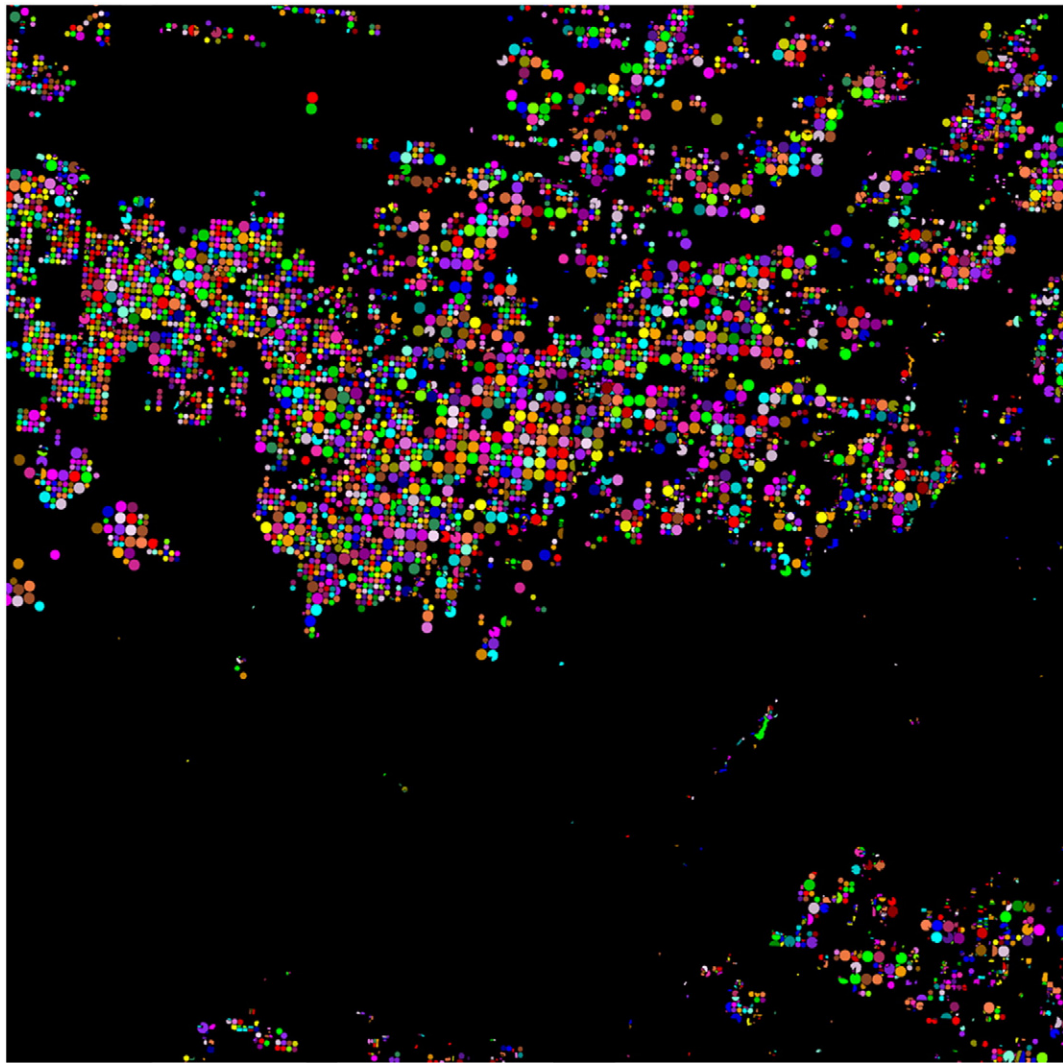


Fig. 11. Crop field extraction results for the Texas tile, 5000 × 5000 30 m pixels, WELD tile h13v12 (35.22669069° to 36.47820154° North, 101.16169227° to 102.94032758° West), in the Northern High Plains in the Northern Texas Panhandle. The colors denote different field segment labels. Black shows locations where no fields were extracted.

field (colored yellow, area 1.61 km²) near the center in the northwest quarter, that was classified as “Woody Wetlands” in the three annual CDL products and is in the Cibola National Wildlife Refuge. Similarly, further south along the Colorado River there are some smaller field extraction commission errors with the same CDL classification.

The majority of the extracted Californian fields are rectangular although circular center-pivot irrigation fields were extracted in the south of the tile. Fig. 18 shows a histogram of the extracted field areas. Nearly three times as many fields were extracted in the Californian tile compared to the Texas tile but the California field areas were typically this multiplier smaller. A total of 16,674 fields with areas ranging from 0.0018 km² to 2.4291 km² and a median area of 0.1197 km² were extracted. Only 0.6% of the fields had areas less than or equal to 16 Landsat pixels, a similar percentage as for the Texas field extraction. The California histogram exhibits peaks at around 0.109 km², 0.234 km², and 0.526 km². Some of the larger fields are circular center-pivot irrigation fields, however, if we assume square field shapes, then the largest cluster area (0.526 km²) and the median field area (0.1197 km²) provide fields with side lengths of 725 m and 346 m, respectively.

Fig. 19 shows a California subset and illustrates the ability of the methodology to extract rectangular shaped fields. The extracted fields and the annual 2008, 2009 and 2010 Cropland Data Layer (CDL)

products are illustrated for the same 21 × 27 km subset dimensions as the Texas subset (Fig. 15). In the Californian subset the predominant field orientations are aligned north-south and east-west but they appear tilted because of the continental WELD Albers projection. Fig. 19 shows crop fields encompassing the cities of Calipatria and Brawley located on the western side of the tile. Between the cities (gray CDL pixels) a series of lakes are evident, and these and the two cities are detected correctly with no fields. The three annual CDL products reveal complex crop rotations and are quite noisy which is unsurprising given that 26 crops were classified although only eight types were classified for more than 0.5% of the subset pixels over the three years.

4.3. South Dakota

Fig. 20 shows the crop field extraction results for the 150 × 150 km South Dakota WELD tile. This tile encompasses the boundaries of the western Corn Belt, the northern Plains, and the Lake States which have the greatest cropland acreage in the conterminous United States (Nickerson, Ebel, Borchers, & Carriazo, 2011). Agriculture occupies the majority of the tile and is primarily intensive commodity crop production with few irrigated fields. Some of the marginal agricultural land is in the Conservation Reserve Program that provides financial incentives for farmers to retire land to native grasses or trees usually for ten years

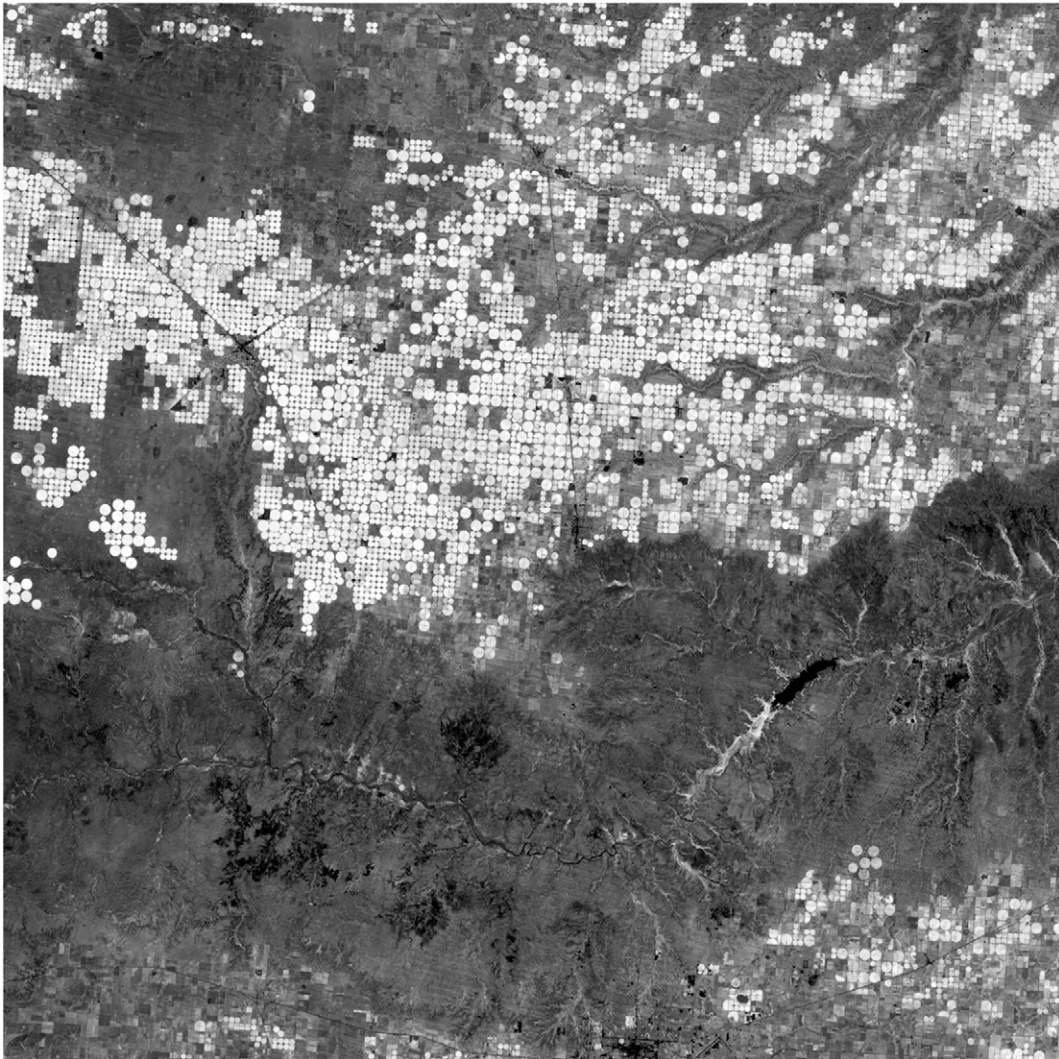


Fig. 12. Crop probability map for the Texas 5000 × 5000 30 m pixel WELD tile derived by Eqs. (1) and (2) from 5-years of weekly WELD products (2006 to 2010).

in duration (Johnson & Maxwell, 2001). The tile pixel locations where no fields were extracted (black) are primarily lakes, cities or towns. The city of Sioux Falls is evident by the extensive black area in the S.E. tile corner and the town of Brookings is evident by the black region about 95 km (2/3rds of the tile dimension) north of Sioux Falls. The historical pattern of 1 × 1 mile road sections with full and quarter section fields that date from the homesteading of the U.S. Midwest (Pitts & Badhwar, 1980) are apparent. A total of 65,727 fields were extracted, about three and nine times more than extracted from the Texas and California tiles, respectively, reflecting the extent of the agriculture across the South Dakota tile. The extracted field areas ranged from 0.0009 km² to 6.6231 km² and the field size histogram (not shown) exhibited peaks at 0.051 km² and 0.526 km². The histogram peak of 0.526 km² was also found for the California results (Fig. 18). If we assume square fields, then this peak (0.526 km²) and the median field area (0.1053 km²) provide South Dakota fields with side lengths of 725 m and 325 m, respectively. There are a minority of very large fields, 22 fields with areas >3 km², and two fields with areas >6 km². These large field areas are not unfeasible and, for example, field sizes with maxima greater than 1500 acres, i.e., greater than 6 km², were reported by Ferguson et al. (1986). This is explored in more detail below.

Fig. 21 shows extracted fields and the annual 2008, 2009 and 2010 CDL products for a 21 × 27 km subset containing the town of Brookings. The predominant crop/soybean agricultural rotation is apparent in the CDL data. The CDL data have less evident classification noise than

observed in the same sized Texas (Fig. 15) and California (Fig. 19) subsets. This may be because the South Dakota subset contains fewer CDL classes (a total of 15 classes with six classified for more than 0.5% of the pixels over the three illustrated years). Most CDL classification noise appears to be related to confusion between the “Other Hay/Non Alfalfa” (dark lime green) and the “Grassland Herbaceous” (light lime green) CDL classes which is a known issue (Johnson, 2013). These two grass type classes occur mainly on marginal agricultural land, particularly low lying land that is prone to flooding and on land around Brookings that is owned by the University and/or is zoned for future building. As in the California and Texas subsets, the extracted fields appear coherent and qualitatively show a visual correspondence with the CDL data. In particular the historical pattern of 1 × 1 mile road sections imposes a clear structure on the extracted fields. However, for the South Dakota subset there are only three sections extracted as complete fields (Fig. 21 a) and only a minority of the sections are composed of a single crop in any of the three years of CDL data (Fig. 21b–c).

To investigate the crop field extraction results in more detail, Fig. 22 shows a 500 × 500 30 m pixel crop field edge presence probability map, and two cloud-free Summer Landsat true color reflectance images sensed in 2008 and 2010. This area was selected as the authors drive through it on a near daily basis. The roads defining the boundaries of the 1 × 1 mile sections and the I-29 interstate running north–south through Brookings in the west of the subset are clearly evident. The majority of the roads have two

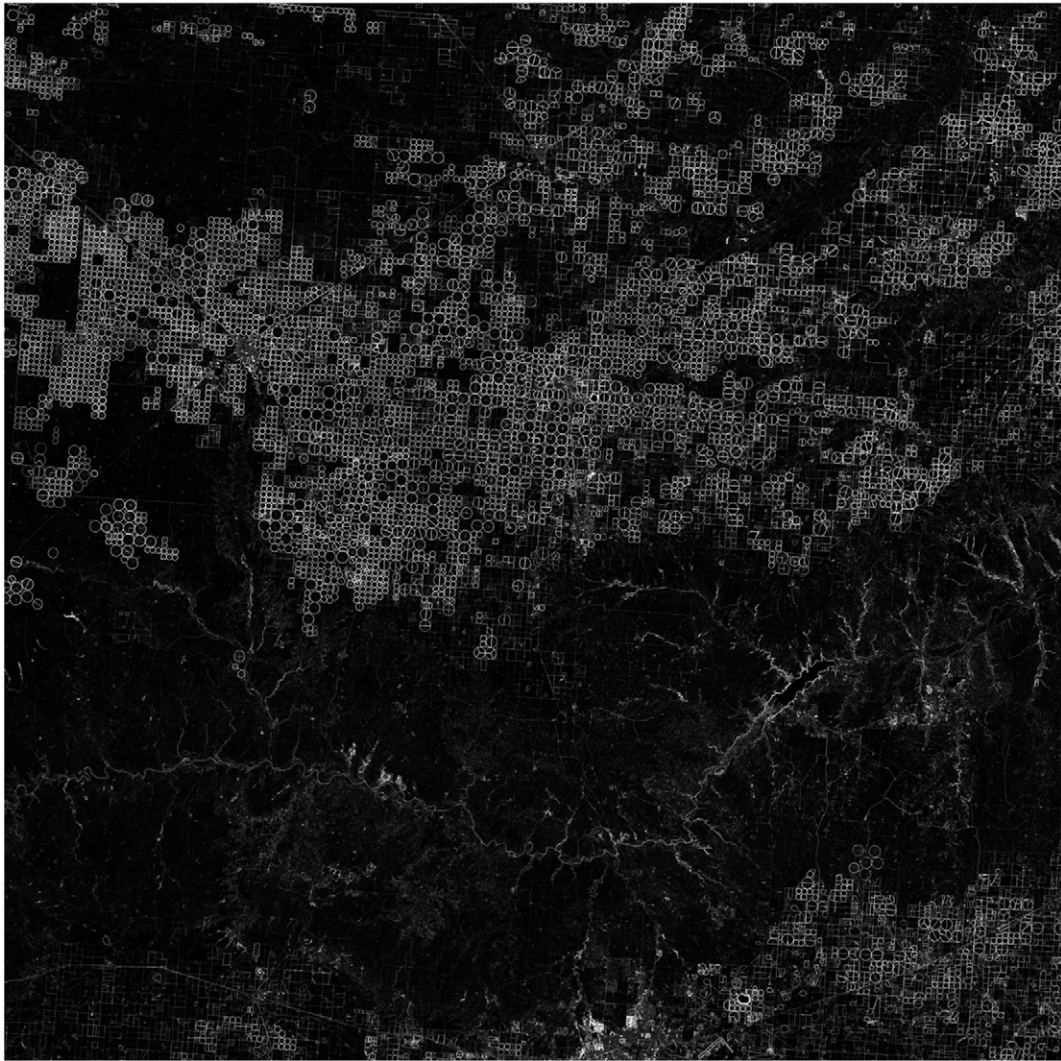


Fig. 13. Crop field edge presence probability map for the Texas 5000 × 5000 30 m pixel WELD tile derived by Eq. (6) from 5-years of weekly WELD products (2006 to 2010).

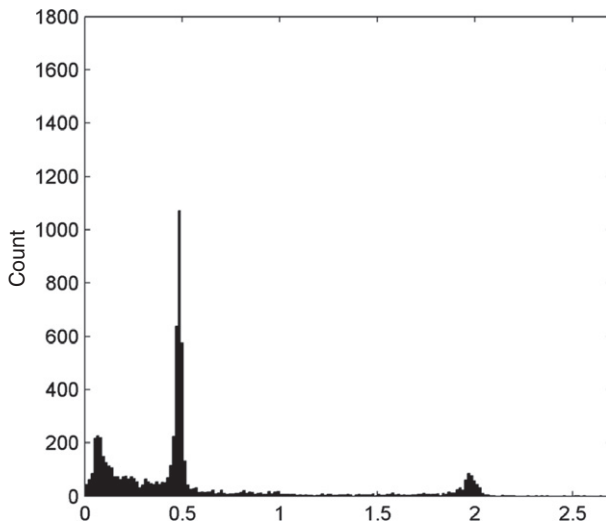


Fig. 14. Histogram of the Texas WELD tile (Fig. 11) field areas. The x-axis (field area) histogram bins are set as an area of 0.0144 km² i.e., an area equivalent to 16 Landsat pixels. A total of 6556 fields were extracted with a median area of 0.4743 km² and with areas ranging from 0.0027 km² to 2.651 km². Note that 1 km² = 100 ha.

lanes with crushed gravel surfaces and are typically less than 10 m wide. Within each 1 × 1 mile section there are usually several fields, one to four farm houses with outbuildings on the field edges, narrow strips of shelter belt trees along a field edge and/or around the farm buildings, and no interior roads. Typically the authors observed no hedge rows between fields within 1 × 1 mile sections, and considerable within-field variability associated with soil and drainage variations.

Fig. 22 illustrates the complexity of the South Dakota agricultural landscape. The crop field edge presence probability map (Fig. 22b) captures much of the detail evident in the two Summer reflectance images (Fig. 22 bottom row). Lower field edge probabilities occur where surface boundaries have changed and where they have low NDVI contrast over the five years of weekly WELD data. These results indicate that although quite small fields can be extracted successfully, e.g., the rectangular east–west oriented field strips in the north, the center and the east of the subset, some of the largest extracted fields should have been extracted as separate fields. For example, the large magenta rectangular field near the center of the subset is usually composed in any single year of separate smaller adjacent fields predominantly of corn and soybean on a two year rotation (Fig. 21b–c). Within the magenta field there are correctly located edges in the field edge presence probability map but they have low probability, most likely because (i) the NDVI

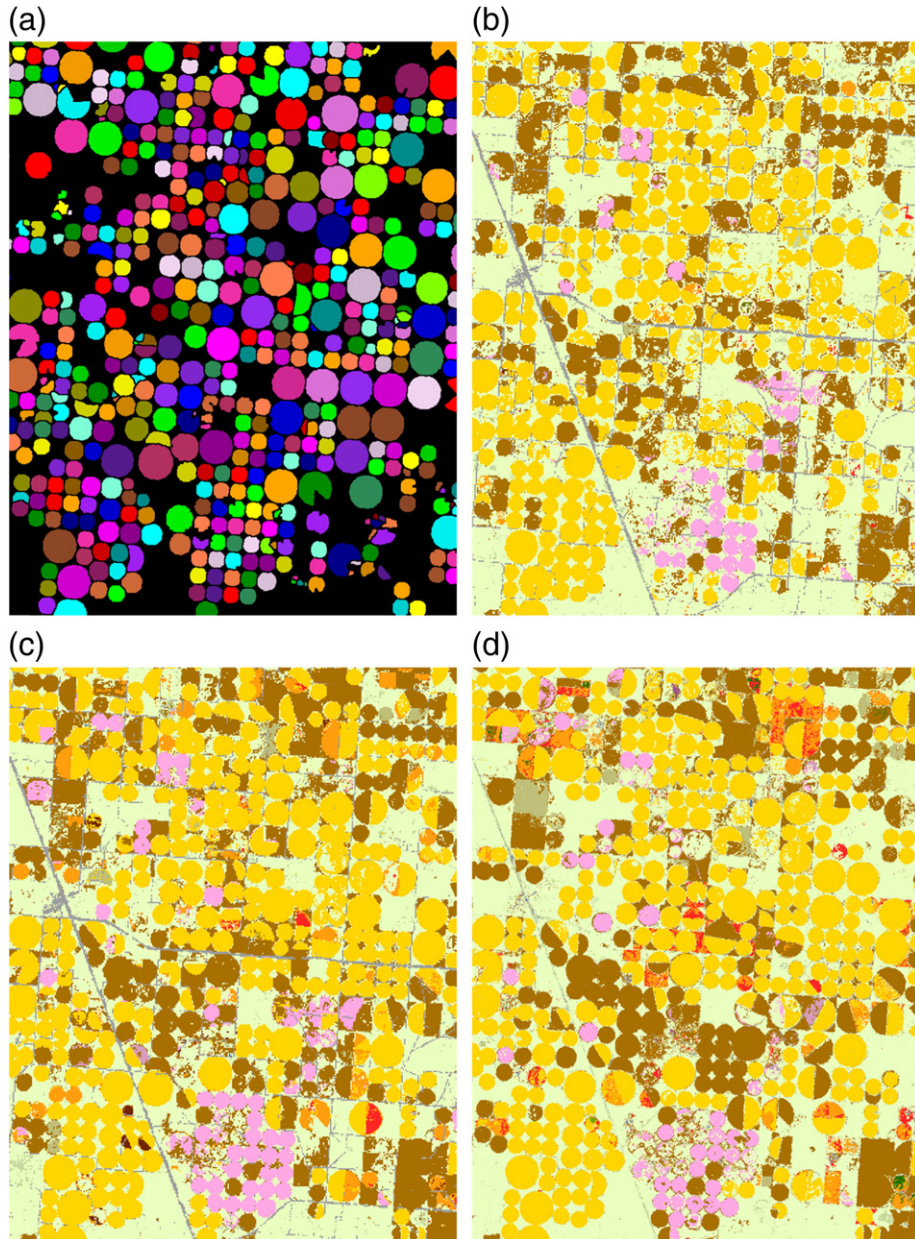


Fig. 15. Texas 700 × 900 30 m pixel subset, including Hartley, TX. (a) Crop field extraction results (Fig. 11); (b) 2008 30 m Crop Data Layer (CDL) classification product, (c) 2009 CDL, (d) 2010 CDL. The annual CDL classifications for this subset included 19 crops where the major ones were Corn, Winter Wheat, Alfalfa, Sorghum and Cotton. The major CDL non-agricultural class (the majority green-yellow background color) is Grassland Herbaceous; developed land (settlements and roads) is shown as gray.

phenology of corn and soybean was sufficiently similar to be indistinguishable, which has been observed by other researchers (Sakamoto et al., 2010), and (ii) because of the smoothing imposed by the rotations occurring over the five years of WELD data. This challenges the field extraction methodology. In addition, some of the roads are so narrow that they do not provide a sufficiently high edge probability between fields planted with the same crop in the same year. This is evident for the moderate size blue rectangular field in the north east of the 500 × 500 pixel subset. Conversely, the majority of the small roads, and also many of the small streams, that are apparent in the reflectance data (Fig. 22 bottom row) divide sections into separate fields and they appear to be extracted correctly. Finally, most of the marginal grass covered land parcels that are classified as “Grassland Herbaceous” in the CDL data (Fig. 21, light lime green) are seemingly incorrectly extracted as crop fields with irregular boundaries. Our inspection from the ground indicates, that much of this land is Hay, perhaps because as noted

previously these CDL grass classes are difficult to differentiate reliably. Several of these grass fields should be joined together but were split because they are joined by “bottleneck” features that failed to pass the test associated with Eq. (11). Despite these issues and although not a formal validation, these and the other results provide confidence in the field extraction methodology, although for the South Dakota case further algorithm refinement is required.

5. Preliminary illustrative validation

A preliminary validation was undertaken to gain quantitative insights into the field extraction accuracy and to prototype a validation protocol. Satellite product validation is undertaken conventionally by comparison with independent reference data (Justice, Belward, Morissette, Lewis, Privette and Baret, 2000). Field boundaries extracted from Landsat 5 Thematic Mapper (TM) data were used as the free and

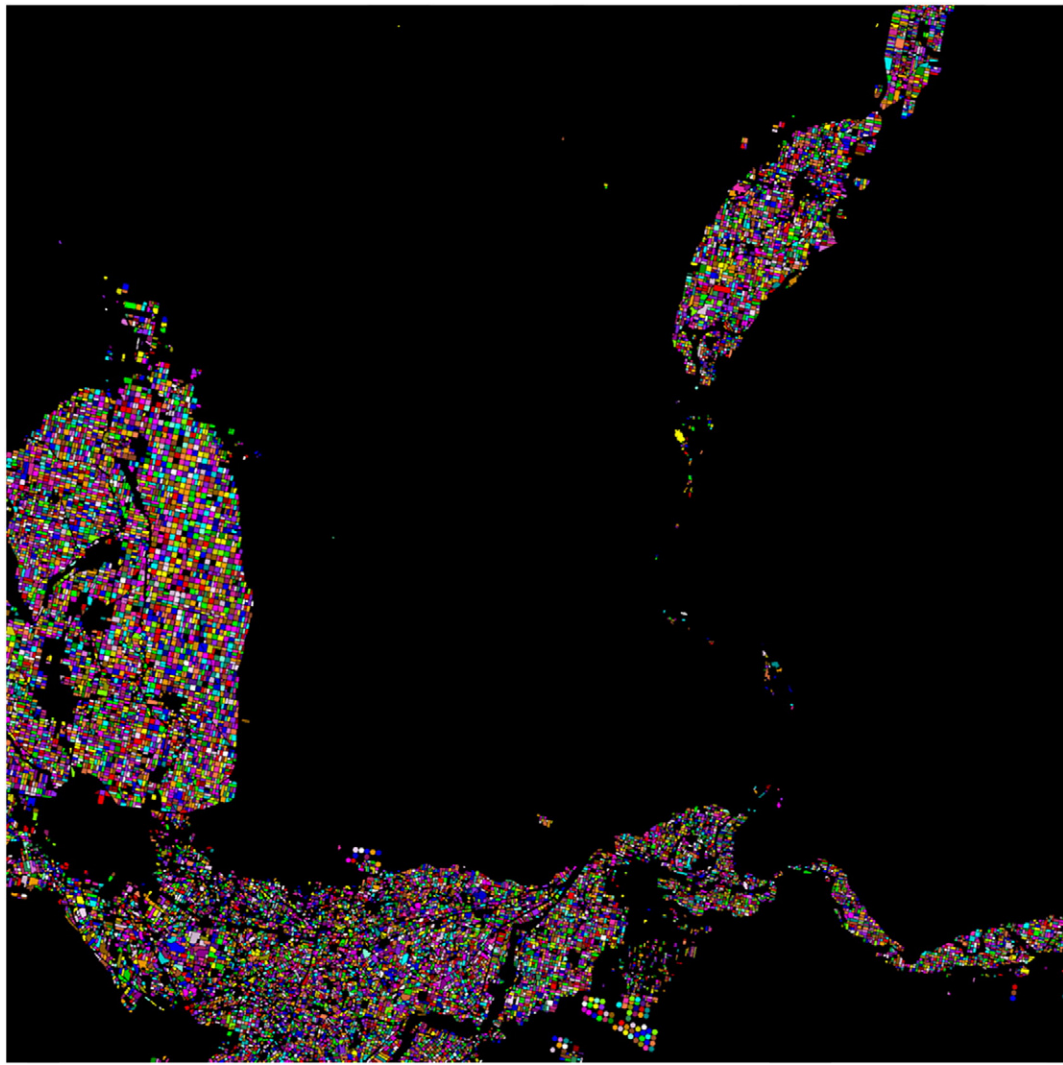


Fig. 16. Crop field extraction results for the California tile, 5000 × 5000 30 m pixels, WELD tile h05v13 (32.58559380° to 33.63728509° North, 113.94813588° to 115.85293402° West), in the south-east corner of California and northern Mexico. The colors denote different field segment labels. Black shows locations where no fields were extracted.

open availability of agricultural field boundary information is limited both nationally and for the three study sites. For example, although national scale field boundaries are annotated annually on aerial photographs as part of the U.S. NASS June survey (Boryan et al., 2011), they are not publically available since the 2008 Food Conservation and Energy Act (USDA, 2008). Validation was undertaken for the California subset (Fig. 19a) due to the availability of peak growing season cloud-free Landsat 5 TM data that provided good field discrimination. A cloud-free March 2010 Landsat 5 TM image was selected. The Landsat 5 TM 30 m red, green and blue visible bands and the 15 m panchromatic band panchromatic band (0.530–0.900 μm) were displayed in two displays. Image-processing software that allowed zooming, local contrast stretching, and rapid comparison of the Landsat 5 TM visible and panchromatic bands was used. An experienced geospatial analyst identified the field boundaries visually and digitized them into a standard polygon vector format with the 15 m pixel precision provided by the panchromatic band. The digitized field boundary polygon coordinates were projected into the WELD Albers projection for comparison with the extracted crop fields.

Fig. 23(a) shows the digitized field boundaries (1456 fields, red vectors) superimposed on the crop field extraction results (1458 fields, white). The fields in these two data sets have a high degree of spatial

correspondence. The majority of fields appear to have been extracted with correct locations, shapes and boundaries. Extracted field objects' commission and omission errors were both less than 1.5% (of the 1458 extracted fields 18 occurred where there were no digitized fields, and of the 1456 digitized fields 17 were not extracted). A minority (3.7%) of the extracted fields were under-split, i.e., fields were extracted as one field but in the digitized field data were composed of several smaller fields, and a minority (8.1%) were over-split, i.e., were extracted as several fields where in the digitized data there was only one field. Close inspection of the data indicated that under-splitting occurred mainly where boundaries within fields were spectrally too weak or impermanent to be extracted. Over-splitting occurred mainly where there were crop rotations within the five years that were not captured by the single Landsat 5 TM image.

The digitized field boundary vector data were rasterized to align with the 30 m crop field extraction results. Conventional accuracy measures to assess pixel level thematic mapping accuracy and to assess the accuracy of areal estimates (Roy & Boschetti, 2009) were derived. A two-way confusion matrix populated with counts of the number of 30 m pixels classified as field or non-field classes in the extracted and the digitized field data was used to derive percent correct and class user's and producer's accuracy statistics (Foody, 2002). The resulting percent

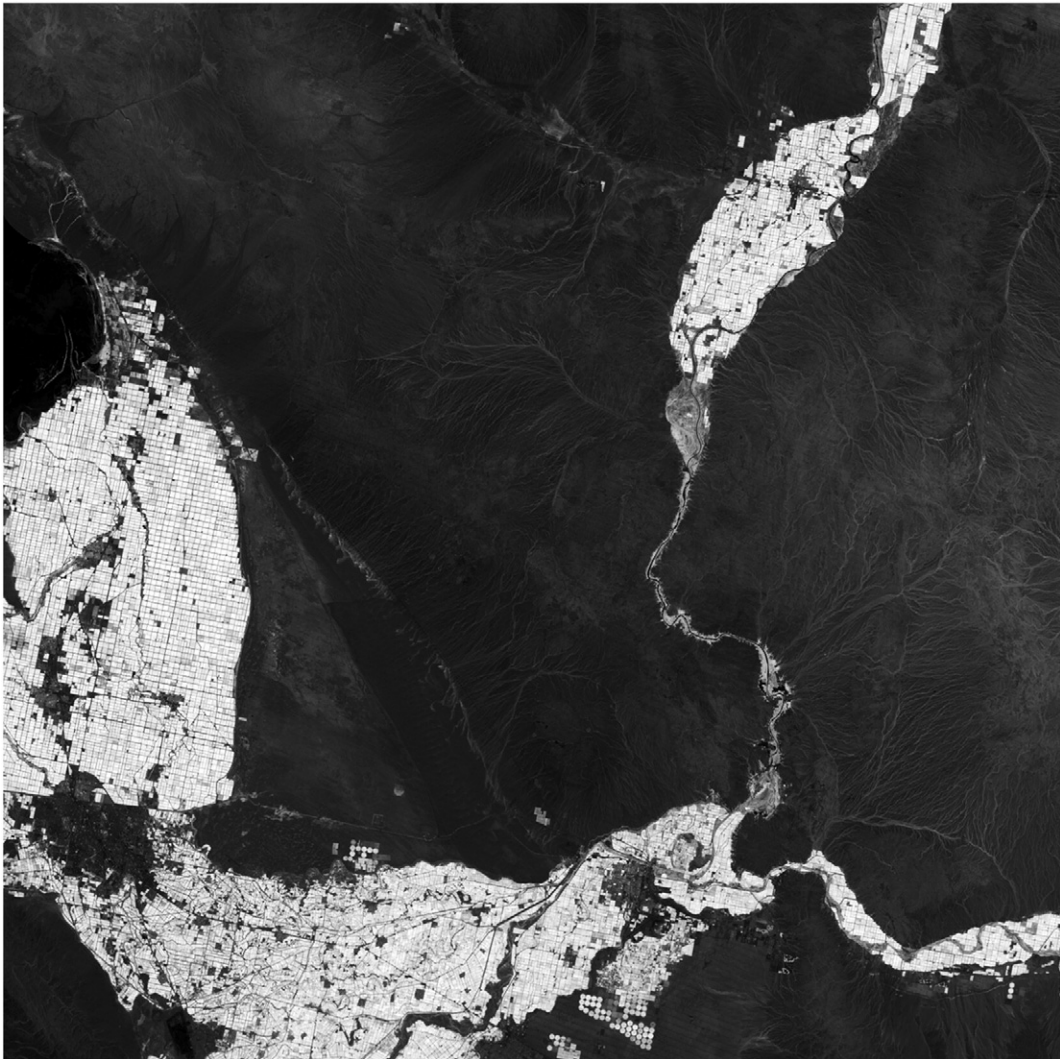


Fig. 17. Crop probability map for the California 5000 × 5000 30 m pixel WELD tile derived by Eqs. (1) and (2) from 5-years of weekly WELD products (2006 to 2010).

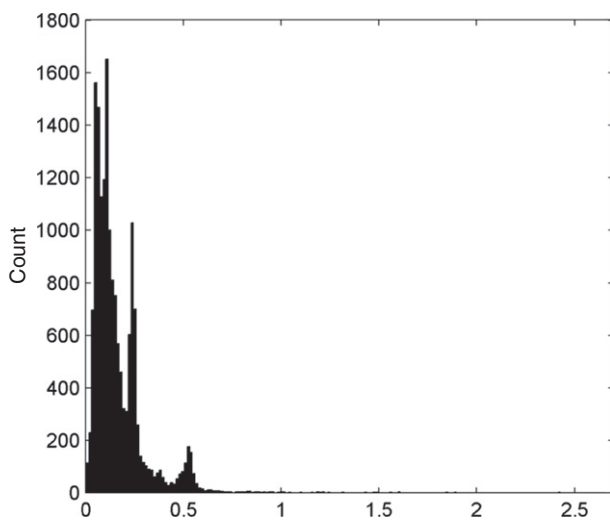


Fig. 18. Histogram of the Californian WELD tile (Fig. 16) field areas. Shown with the same axes range and binning scale as the Texas histogram (Fig. 14). A total of 16,674 fields were extracted with a median area of 0.1197 km² and with areas ranging from 0.0018 km² to 2.4291 km². Note that 1 km² = 100 ha.

correct accuracy was 90.1%, and the user's and producer's accuracies were 83.0% and 93.8% for the field class and 95.7% and 87.7% for the non-field class, respectively. The areas of individual fields in the extracted and the digitized field data were derived and their differences were compared considering only the 1284 fields that had a one-to-one relationship, i.e., only extracted and digitized fields that intersected exclusively with one another were considered. The individual field area data were highly correlated with an ordinary least squares linear relationship of the form: extracted field area = 0.9745 × digitized field area - 0.0098 (km²) ($R^2 = 0.97$).

The above conventional validation results document accurate field extractions. However, they do not quantify the extraction accuracy of individual fields. Inspection of Fig. 23(a) indicates that the extracted and digitized fields were sometimes imperfectly aligned and that extracted fields were smaller or larger than in the digitized field data. Geometric measures were applied to quantify these individual field extraction errors and the results are illustrated in Fig. 23(b)–(c) and are explained below.

A metric to quantify the degree of misalignment of the extracted fields with respect to the digitized fields was defined as:

$$L(E_j; T_i) = \sqrt{(x_{Ej} - x_{Ti})^2 + (y_{Ej} - y_{Ti})^2} \quad (14)$$

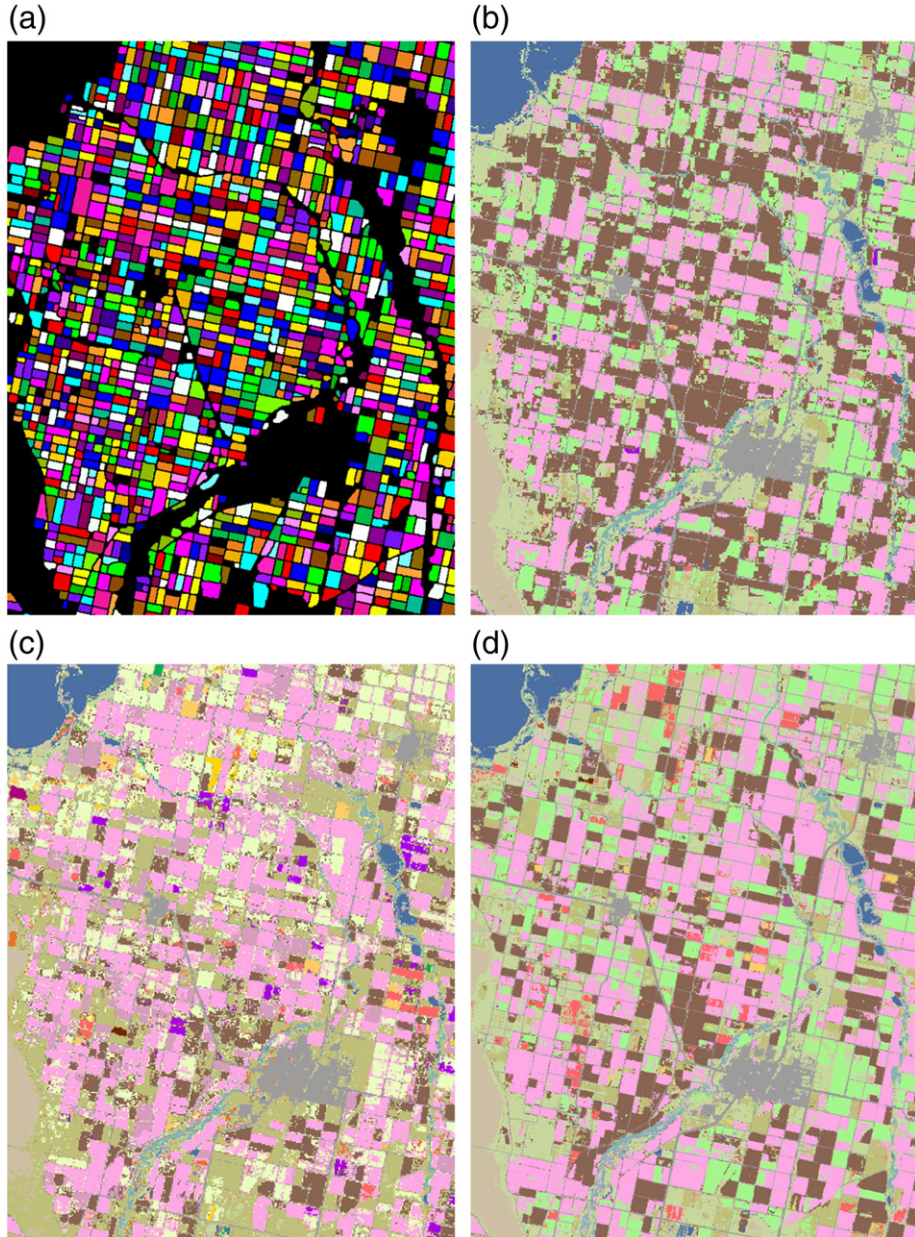


Fig. 19. California 700×900 30 m pixel subset including the cities of Calipatria (northeast) and Brawley (central). (a) Crop field extraction results (Fig. 16); b) 2008 30 m Crop Data Layer (CDL) classification product, (c) 2009 CDL, (d) 2010 CDL. The annual CDL classifications for this subset included 26 crops where the major ones were Durum Wheat, Alfalfa, Other Hay/Non Alfalfa, and Lettuce. The major CDL non-agricultural classes (brown/gray shades) are Fallow/Idle cropland, Barren, and Shrubland; developed land (settlements and roads) is shown as gray.

where (x_{Ej}, y_{Ej}) and (x_{Ti}, y_{Ti}) are the centroids of corresponding fields E_j and T_i , respectively, T is the set of the digitized raster fields considered as “truth”, and E is the set of the extracted fields. Ideally, the extracted and digitized field boundaries would align perfectly. However, the rasterized digitized fields may have sub-pixel boundary imprecision due to the vector to raster conversion process, and the boundaries of a correctly extracted field may be imprecise due to sub-pixel Landsat 5 and 7 geolocation errors (Lee et al., 2004). The field centroid is defined as the arithmetic mean position of all the pixels in the field and so L is not expected to be biased by these random sources of imprecision. If an extracted field E_j intersected with more than one field in T then the location error was computed as the weighted sum of the L values computed for each T field weighted by the intersection area of E_j and the T field. For example, if E_j intersected both T_1 and T_2 , then $L(E_j; T_1, T_2) =$

$(L(E_j, T_1) \times |E_j \cap T_1| + L(E_j, T_2) \times |E_j \cap T_2|) / (|E_j \cap T_1| + |E_j \cap T_2|)$. Fig. 23(b) shows the extracted field centroid misalignment L values. For convenience the gray colors show fields that were present in the extracted or the digitized truth data but not in both and so illustrate where L could not be computed. The minimum and mean L values were 0.01 and 1.36 pixels, respectively, and the median L value was 0.71 pixels. The mean and median misalignment of the fields is about 41 m and 21 m, respectively, which is comparable to a Landsat 30 m pixel dimension. A minority of 148 fields had L values greater than 3 pixels (yellow to red colors) with a maximum L of 18.81 pixels. These however mainly occurred where the extracted fields were over- or under-split.

Metrics to quantify the degree that an extracted field was under- or over-segmented, i.e., was larger or smaller, respectively, than the

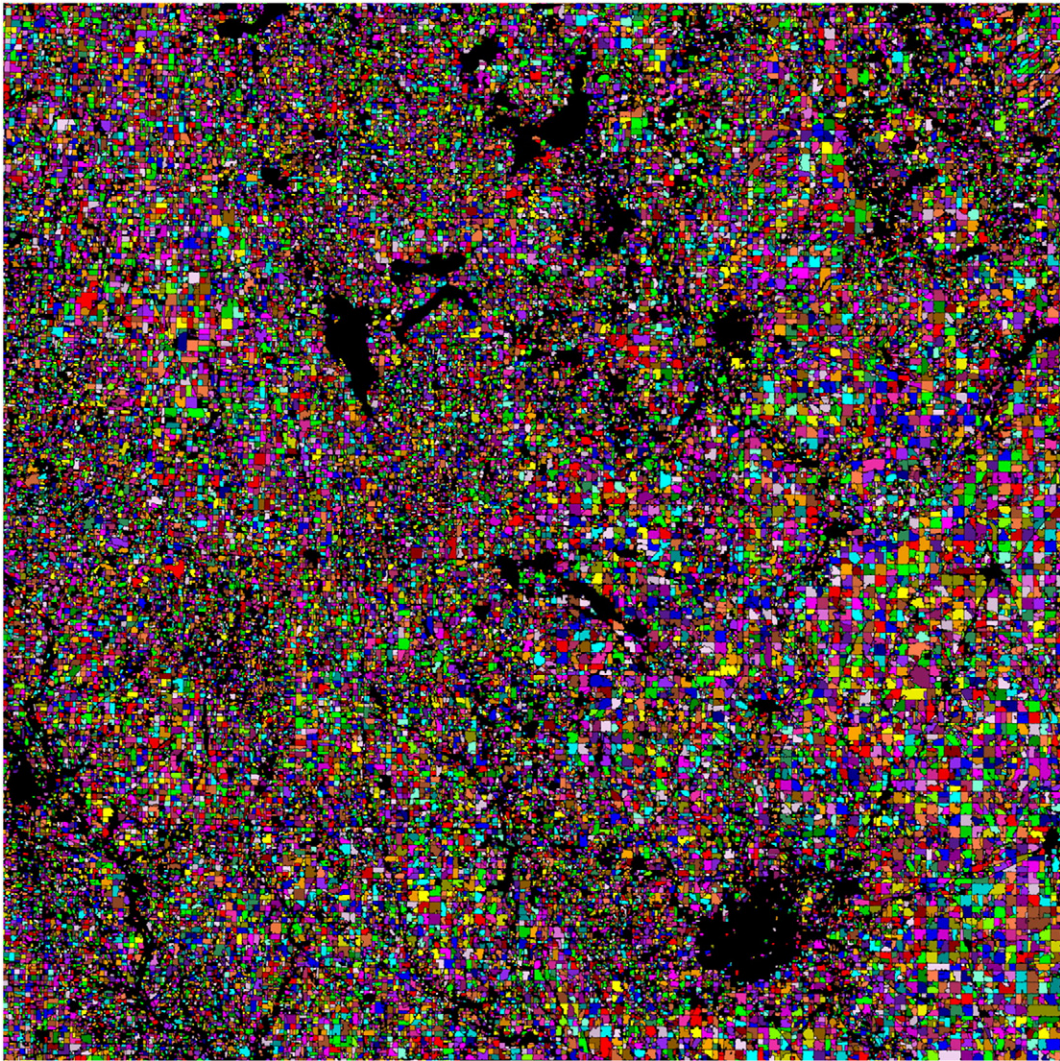


Fig. 20. Crop field extraction results for the South Dakota tile, 5000 × 5000 30 m pixels, WELD tile h16v06 (43.37681588° to 44.70557124° North, 96.19343546° to 98.0936587° West), predominantly covering central eastern South Dakota and parts of western Minnesota and N.W. Iowa. The colors denote different field segment labels. Black shows locations where no fields were extracted.

digitized field data, were defined (Persello & Bruzzone, 2010). The degree of under-segmentation of an extracted field E_j was defined:

$$S^{\text{under}}(E_j; T_i) = \left(1 - \frac{|T_i \cap E_j|}{|E_j|}\right) \times 100\% \quad (15)$$

Conversely, the degree of over-segmentation of an extracted field E_j was defined:

$$S^{\text{over}}(E_j; T_i) = \left(1 - \frac{|T_i \cap E_j|}{|T_i|}\right) \times 100\% \quad (16)$$

As for the computation of L (Eq. (14)), if E_j intersected with multiple fields in T , or if T_i intersected with multiple fields in E , then the value of Eq. (15) or (16) was computed as the sum of the S values computed for each intersecting field weighted by the corresponding intersection areas. These metrics provide percentage values ranging from 0% to 100%. Fig. 23(c) and (d) illustrate the results with gray colors showing fields that were present in the extracted or the digitized truth data but not in both. The greatest S^{under} and S^{over} values were 83.1% and 83.5%, respectively, and occurred where the extracted fields were over- or

under-split. The mean S^{under} and S^{over} values were 5.7% and 14.2%, respectively. The relatively larger mean S^{over} value indicates that on average the extracted fields were smaller than in the digitized data. This pattern was also observed in the less than unity regression slope between the extracted and digitized field areas, i.e. extracted field area = $0.9745 \times$ digitized field area – 0.0098 (km^2). This occurs due to the initial VRGAC segmentation that was implemented to trim the initial segment boundaries (Section 3.4) and explains why the smaller extracted fields tend to have larger S^{over} values (Fig. 23(c)).

The three geometric measures were even smaller when they were only applied to the 1284 fields that had a one-to-one relationship. The mean L , S^{under} and S^{over} values were 0.70 pixels, 4.0%, and 12.8%, respectively, which indicated high individual crop field extraction accuracy.

6. Discussion and conclusions

This paper has presented an automated computational methodology to extract agricultural crop fields from Web Enabled Landsat data (WELD) time series. Qualitatively the results for WELD tiles encompassing rectangular, circular (center-pivot irrigation) and irregularly shaped fields in Texas, California and South Dakota are promising, certainly when compared to the original input weekly WELD data and to

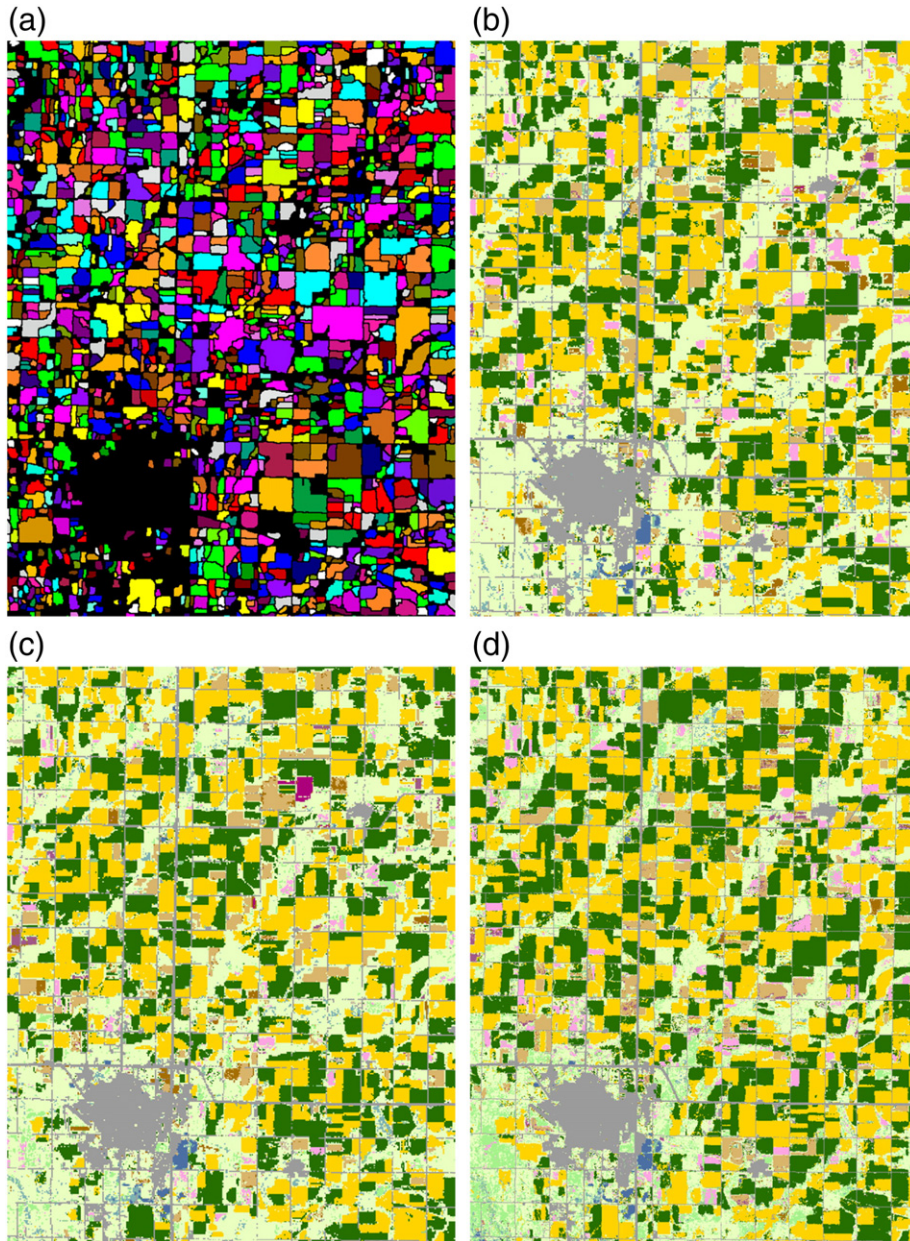


Fig. 21. South Dakota 700 × 900 30 m pixel subset near Brookings (shown by gray CDL pixels). (a) Crop field extraction results (Fig. 20); b) 2008 30 m Crop Data Layer (CDL) classification product, (c) 2009 CDL, (d) 2010 CDL. The annual CDL classifications for this subset included 15 crops where the major ones were Corn, Soybean, Spring Wheat, Alfalfa and Other Hay/Non Alfalfa shown as dark lime green. The major CDL non-agricultural class is Grassland Herbaceous shown as light lime green.

independent United States Department of Agriculture (USDA) National Agricultural Statistics Service (NASS) cropland data layer (CDL) classifications. Coherent fields that are visually apparent were extracted with relatively limited apparent errors of omission or commission, although the results for the more complex South Dakota data appeared less reliable. A preliminary validation was undertaken for the California subset to gain quantitative insights into the field extraction accuracy and to prototype a validation protocol. Independent field boundaries digitized manually from Landsat 5 Thematic Mapper (TM) data were compared with extracted crop fields. Conventional accuracy measures to assess pixel level thematic mapping accuracy provided a 90.1% overall accuracy with field class user's and producer's accuracies of 83.0% and 93.8%. Geometric measures of the misalignment of field centroids and the degree of over- or under-segmentation were developed and applied to quantify the extraction accuracy of individual fields. These indicated that the extracted fields

were on average less than 15% smaller than in the digitized data and that the extracted field centroids were misaligned relative to the digitized equivalent by about one 30 m pixel. Summary statistics of these geometric measures and their spatially explicit representation provide individual field extraction accuracy information and are recommended for incorporation into a more comprehensive validation. Future research to use multi-temporal remotely sensed data to identify fields and delineate their boundaries through the growing season is also recommended to provide improved independent reference data.

Crop field extraction omission errors are inevitable due to the limited spatial resolution of the satellite data and satellite geolocation errors (Duveiller & Defourny, 2010; Ozdogan & Woodcock, 2006; Roy, 2000). These factors limit the ability to extract reliably small and spatially fragmented fields and also cause omission errors at field boundary corners with acute angles, and reduce the ability to locate field edges to

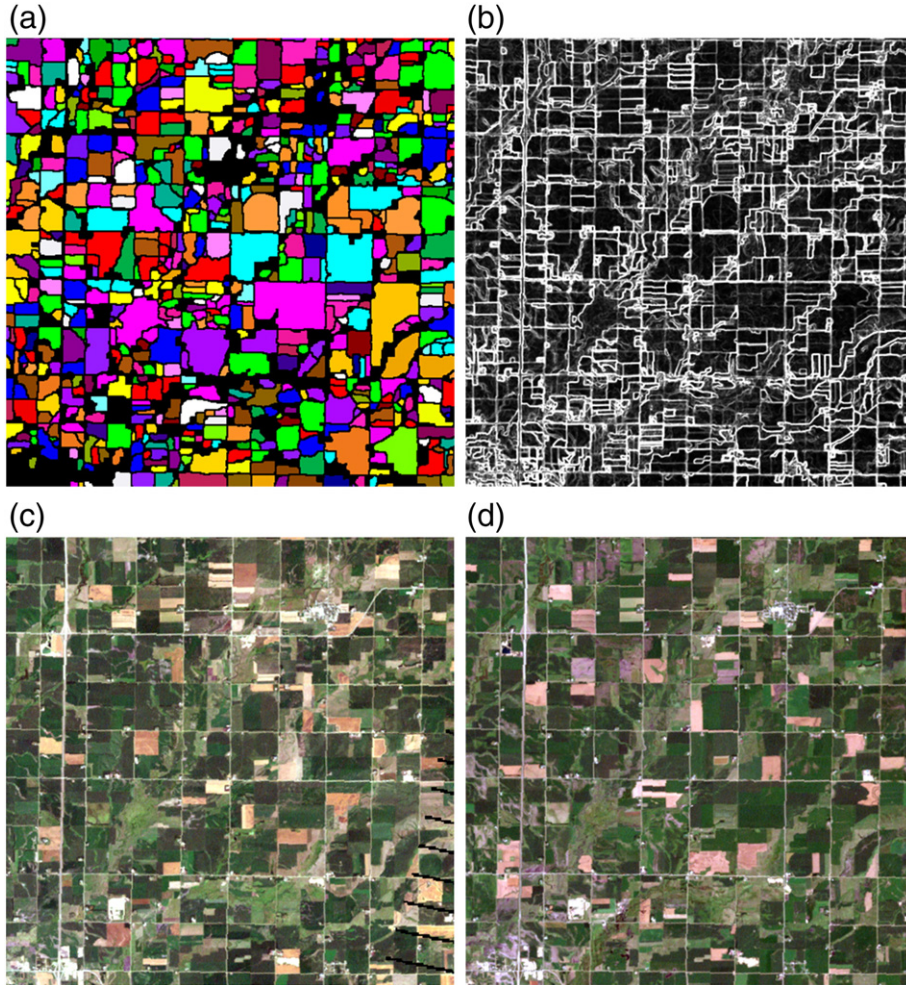


Fig. 22. Detail of a 500×500 30 m pixel subset of the N.E. corner of Fig. 21 including the towns of Brookings (S.E. corner) and White (N.E. quadrant). (a) Crop field extraction results; (b) Crop field edge presence probability map derived by Eq. (6) from 5-years of weekly WELD products (2006 to 2010). (c) WELD August 7th 2008 true color top of atmosphere reflectance. (d) July 28th 2010 reflectance.

sub-pixel precision. In this study fields composed of less than 16 30 m Landsat pixels were considered conservatively to be extracted unreliable. However, this minimum area threshold is based more on our algorithm development experience than a rigorous quantitative assessment. The level set function approach used by the variational region-based geometric active contour (VRGAC) segmentation is non-linear and not amenable to analytical error analysis (Osher & Sethian, 1988). Consequently, a sensitivity analysis using synthetic field shapes is required to quantify the minimum area and shape characteristics that can be extracted reliably. Other forms of omission errors include adjacent fields with indistinct boundaries, for example, narrow roads with dimensions not larger than a Landsat pixel dimension, such as observed in the South Dakota results, that may not be extracted as separate fields but rather as single fields. Further, when a field is planted with more than one crop but no physical separating boundary it may not be extracted reliably into several fields if the crops have similar NDVI phenology. In addition, although not observed in this study, crop fields that have low amplitude NDVI phenology, such as, for example, crops with low canopy density and/or low leaf area, may not be extracted reliably.

Crop field extraction commission errors were observed for field objects that were labeled in the NASS CDL products as "Woody Wetlands". Wetlands can be spectrally confused with other vegetation types including agricultural crops and forests (Ozesmi & Bauer, 2002). The commission errors occurred, however, because the crop probability map generation assumed that pixels with consistently high seasonal NDVI

values are likely to be crops. Non-agricultural vegetated areas, such as forests, grasslands and pastures, may also have high seasonal NDVI phenology, and if they have distinct boundaries they are likely to be incorrectly extracted as crop field objects. Similarly, rainfed agricultural regions may have less boundary contrast with non-agricultural land covers. Future research to remove these commission errors is required. The phenology of crops, forests, and grasslands may be sufficiently different to afford discrimination based on more sophisticated understanding of crop phenologies and a more sophisticated crop probability map generation. Other potential solutions include the application of texture metrics and geometric information concerning the spatial characteristics and neighborhood relationships of fields. The most straightforward solution, however, is to mask the commission errors with existing 30 m land cover products that define forest and grassland classes, such as the National Land Cover Database (Fry, Xian, Jin, Dewitz, Homer, Limin, et al., 2011) or the NASS cropland data layer (Johnson & Mueller, 2010), and to use some form or majority filter of the land cover classified pixels within each field object.

Crop field extraction errors will occur if crop field boundaries are physically moved during the Landsat time series acquisition period. For example, this was observed for overlapping circular center-pivot irrigation fields in the Texas subset and is a fundamental change detection issue. Using a shorter Landsat time series, for example, three years of data instead of five, may reduce the likelihood of occurrence of this issue but will provide fewer opportunities for uncontaminated Landsat surface observations. Instead, using contemporaneous Landsat 5

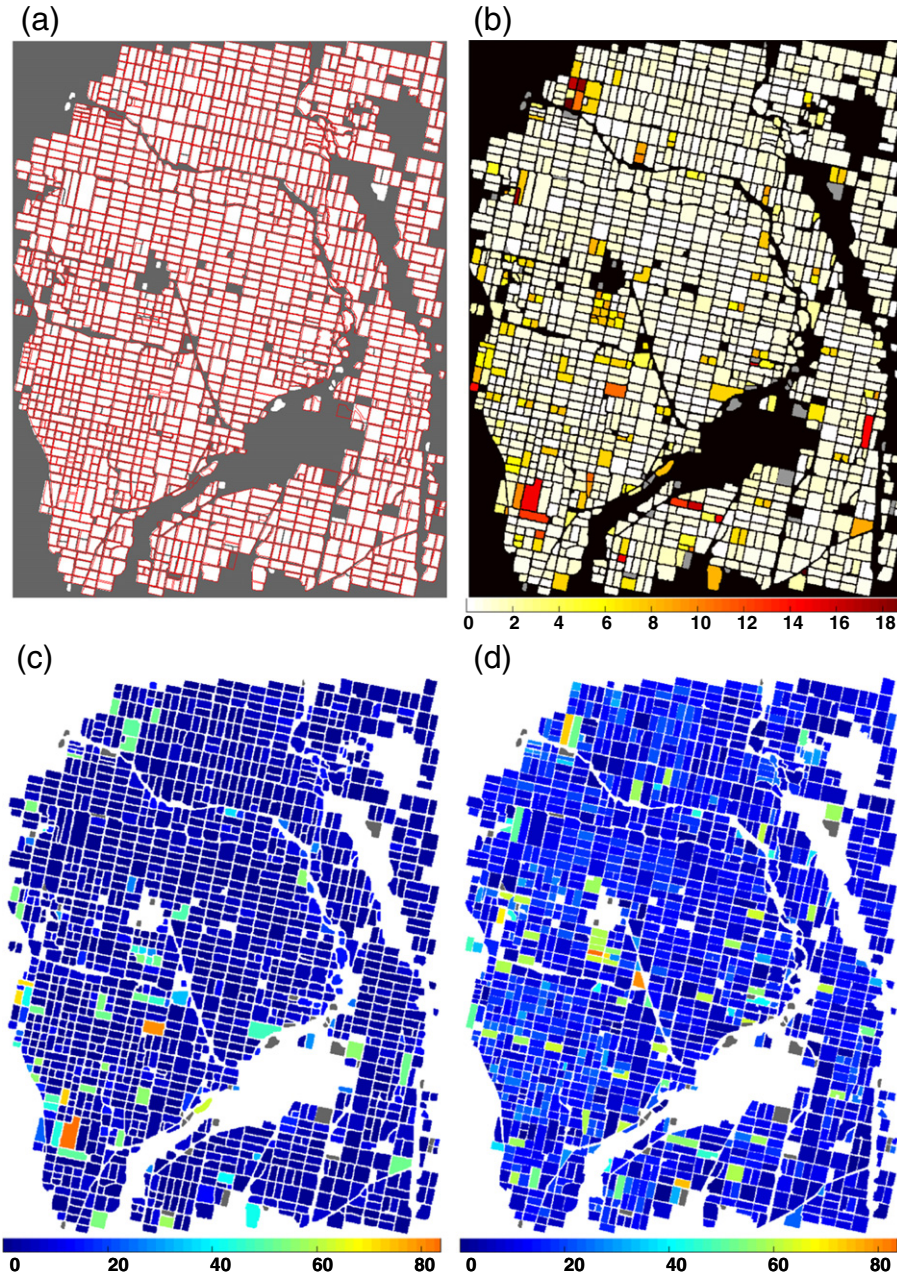


Fig. 23. Validation results for the California subset. (a) extracted crop fields (white, the same as Fig. 19(a)), gray no extracted crop fields, independent Landsat 5 TM digitized field boundaries superimposed (red vectors); fields that intersected the California subset edges were removed, (b) the individual field centroid misalignment metric (L) defined in units of 30 m pixels, (c) the individual field under-segmentation metric (S_{under}) (0.0–83.1%), (d) the individual field over-segmentation metric (S_{over}) (0.0–83.5%). In (b)–(d) gray show fields that were present in the extracted or the digitized truth data but not in both.

Thematic Mapper and Landsat 7 ETM+ data, which have the same sensing capabilities but are sensed eight days apart and so provide more cloud-free surface observation opportunities within any time period (Kovalsky & Roy, 2013), is recommended.

The spatially explicit crop probability and field edge presence products that were generated as intermediate products by the described methodology are potentially useful themselves for agricultural and other land cover land use monitoring applications. For example, the crop field edge probability map captured not only field edges but also the edges of certain water bodies and roads that were adjacent to vegetation which suggests that the methodology could be adapted to detect these feature types. Further, with refinement, other land use objects such as areas of forestry and grasslands could potentially be extracted.

To date, studies of the incidence, drivers and impacts of changing field sizes have not been undertaken over large areas because consistently processed appropriate resolution data have not been available or affordable and because of computational constraints. Seminal work to compute agricultural field size histograms was undertaken by visual interpretation of more than 100,000 fields using Landsat data acquired over parts of Canada and the Midwestern U.S. (Ferguson et al., 1986). The free availability of Landsat data and the WELD processing reduces data access and cost constraints. Moreover, computer processing capabilities are improving rapidly. Although the methodology described in this paper is computationally intensive compared to supervised classification approaches that have been applied to WELD data (Hansen et al., 2011; Hansen et al., 2014), it is sufficiently efficient and structured to be

scalable to continental application. The field extraction methodology was implemented in a fully automated and computationally efficient manner in the C compiled computer language and applied on a WELD tile by tile basis. Calculation of the probability of crop and field edge presence took ~15% of the processing time, VRGAC segmentation ~50%, decomposition of connected segments belonging to multiple fields into coherent isolated field segments ~5%, detection and association of parts of circular fields ~25%, and the final morphological segment cleaning less than 5% of the processing time. Processing multiple WELD tiles in parallel would reduce the processing time proportionally. Future research will be to further test the applicability of the crop field extraction methodology at different locations, validate the results using the conventional and the new per-field accuracy measures demonstrated in this paper, and refine the algorithm as needed for large-area application.

Acknowledgements

This research was funded by NASA NNN09ZDA001N-LCLUC (grant number NNX11AH99G - NSR 311144). The U.S. Landsat project management and staff at USGS EROS, Sioux Falls, South Dakota, are thanked for provision of the Landsat 7 ETM + data. The USDA management and staff are thanked for provision of the Crop Data Layer classification products. The anonymous reviewers are thanked for their comments that improved this paper.

References

- Allen, J.D. (1990). A look at the remote sensing applications program of the National Agricultural Statistics Service. *Journal of Official Statistics*, 6, 393–409.
- Badhwar, G. D. (1984). Automatic corn-soybean classification using Landsat MSS data, I, Near-harvest crop proportion estimation. *Remote Sensing of Environment*, 14, 15–29.
- Basnyat, P., McConkey, B., Meinert, B., Gatzke, C., & Noble, G. (2004). Agriculture field characterization using aerial photograph and satellite imagery. *IEEE Geoscience and Remote Sensing Letters*, 1, 7–10.
- Bauer, M. E., Hixson, M. M., Davis, B. J., & Etheridge, J. B. (1978). Area estimation of crops by digital analysis of Landsat data. *Photogrammetric Engineering & Remote Sensing*, 44, 1033–1043.
- Becker-Reshef, I., Justice, C., Sullivan, M., Vermote, E., Tucker, C., Anyamba, A., et al. (2010). Monitoring global croplands with coarse resolution earth observations: The Global Agriculture Monitoring (GLAM) project. *Remote Sensing*, 2(6), 1589–1609.
- Benediktsson, J. A., Pesaresi, M., & Arnason, K. (2003). Classification and feature extraction for remote sensing images from urban areas based on morphological transformations. *IEEE Transactions on Geoscience and Remote Sensing*, 41, 1940–1949.
- Bleau, A., & Leon, L. J. (2000). Watershed-Based segmentation and region merging. *Computer Vision and Image Understanding*, 77, 317–370.
- Boryan, C., Yang, Z., Mueller, R., & Craig, M. (2011). Monitoring US agriculture: The US department of agriculture, National Agricultural Statistics Service, cropland data layer program. *Geocarto International*, 26, 341–358.
- Butt, M.A., & Maragos, P. (1998). Optimum design of Chamfer distance transform. *IEEE Transactions on Image Processing*, 7, 1477–1484.
- Carfagna, E., & Gallego, F. J. (2005). Using remote sensing for agricultural statistics. *International Statistical Review*, 73(3), 389–404.
- Caselles, V., Catte, F., Coll, T., & Dibos, F. (1993). A geometric model for active contours in image processing. *Numerische Mathematik*, 66, 1–31.
- Chan, T., & Vese, L. (2001). Active contours without edges. *IEEE transactions on image processing*, 10, 266–277.
- Chang, J., Hansen, M. C., Pittman, K., Carroll, M., & DiMiceli, C. (2007). Corn and soybean mapping in the United States using MODIS time-series data sets. *Agronomy Journal*, 99, 1654–1664.
- Davies, E. R. (1987). A high speed algorithm for circular object detection. *Pattern Recognition Letters*, 6, 323–333.
- Definiens eCognition Developer 8 – User guide. (2009). Munchen, Germany Definiens AG, Trappentreustr (1 D-80339).
- Duveiller, G., & Defourny, P. (2010). A conceptual framework to define the spatial resolution requirements for agricultural monitoring using remote sensing. *Remote Sensing of Environment*, 114, 2637–2650.
- Evans, C., Jones, R., Svalbe, I., & Berman, M. (2002). Segmenting multispectral Landsat TM images into field units. *IEEE Transactions on Geoscience and Remote Sensing*, 40, 1054–1064.
- Ferguson, M., Badhwar, G., Chhikara, R., & Pitts, D. (1986). Field size distributions for selected agricultural crops in the United States and Canada. *Remote Sensing of Environment*, 19, 25–45.
- Fisher, J. I., Mustard, J. F., & Vadeboncoeur, M.A. (2006). Green leaf phenology at Landsat resolution: Scaling from the field to the satellite. *Remote Sensing of Environment*, 100, 265–279.
- Foody, G. (2002). Status of land cover classification accuracy assessment. *Remote Sensing of Environment*, 80, 185–201.
- Fry, J. A., Xian, G., Jin, S., Dewitz, J. A., Homer, C. G., Limin, Y., et al. (2011). Completion of the 2006 National Land Cover Database for the conterminous United States. *Photogrammetry Engineering and Remote Sensing*, 77, 858–864.
- Hall, F. G., & Badhwar, G. D. (1987). Signature-extensible technology: Global space-based crop recognition. *IEEE Transaction on Geoscience and Remote Sensing*, 25, 3–103.
- Hansen, M. C., Egorov, A., Potapov, P. V., Stehman, S. V., Tyukavina, A., Turubanova, S. A., et al. (2014). Monitoring conterminous United States (CONUS) land cover change with Web-Enabled Landsat Data (WELD). *Remote sensing of Environment*, 140, 466–484.
- Hansen, M. C., Egorov, A., Roy, D. P., Potapov, P., Ju, J., Turubanova, S., et al. (2011). Continuous fields of land cover for the conterminous United States using Landsat data: First results from the Web-Enabled Landsat Data (WELD) project. *Remote Sensing Letters*, 2, 279–288.
- Hay, G. J., & Castilla, G. (2008). Geographic Object-Based Image Analysis (GEOBIA): A new name for a new discipline? In T. Blaschke, S. Lang, & G. J. Hay (Eds.), *Object-based image analysis – Spatial concepts for knowledge-driven remote sensing applications* (pp. 81–92). Springer–Verlag (Chapter 1.4).
- Holben, B. (1986). Characteristics of maximum-value composite images from temporal AVHRR data. *International Journal of Remote Sensing*, 7, 1417–1434.
- Honkanen, M., Saarenrinne, P., Stoor, T., & Niinimaki, J. (2005). Recognition of highly overlapping ellipse-like bubble images. *Measurement Science & Technology*, 16(9), 1760–1770.
- Huang, X., & Zhang, L. (2008). An adaptive mean-shift analysis approach for object extraction and classification from urban hyperspectral imagery. *IEEE Transactions on Geoscience and Remote Sensing*, 46, 4173–4185.
- Ioannou, D., Huda, W., & Laine, A. F. (1999). Circle recognition through a 2D Hough Transform and radius histogramming. *Image and Vision Computing*, 17, 15–26.
- Jakubauskas, M. E., Legates, D. R., & Kastens, J. H. (2002). Crop identification using harmonic analysis of time-series AVHRR NDVI data. *Computers and Electronics in Agriculture*, 37, 127–139.
- Johnson, D.M. (2013). A 2010 map estimate of annually tilled cropland within the conterminous United States. *Agricultural Systems*, 144, 95–105.
- Johnson, J., & Maxwell, B. (2001). The role of the Conservation Reserve Program in controlling rural residential development. *Journal of Rural Studies*, 17, 3–332.
- Johnson, D.M., & Mueller, R. (2010). The 2009 cropland data layer. *Photogrammetry & Remote Sensing*, 76, 1201–1205.
- Ju, J., & Roy, D. P. (2008). The availability of cloud-free Landsat ETM + data over the conterminous United States and globally. *Remote Sensing of Environment*, 112, 1196–1211.
- Ju, J., Roy, D. P., Vermote, E., Masek, J., & Kovalskyy, V. (2012). Continental-scale validation of MODIS-based and LEDAPS Landsat ETM + atmospheric correction methods. *Remote Sensing of Environment*, 122, 175–184.
- Justice, C., Belward, A., Morisette, J., Lewis, P., Privette, J., & Baret, F. (2000). Developments in the validation of satellite products for the study of the land surface. *International Journal of Remote Sensing*, 21(17), 3383–3390.
- Kovalskyy, V., & Roy, D. P. (2013). The global availability of Landsat 5 TM and Landsat 7 ETM + land surface observations and implications for global 30 m Landsat data product generation. *Remote Sensing of Environment*, 130, 280–293.
- Kovalskyy, V., Roy, D. P., Zhang, X., & Ju, J. (2011). The suitability of multi-temporal Web-Enabled Landsat Data (MODIS) NDVI for phenological monitoring – A comparison with flux tower and MODIS NDVI. *Remote Sensing Letters*, 3, 325–334.
- Lankton, S., & Tannenbaum, A. (2008). Localizing region-based active contours. *IEEE Transactions on Geoscience and Remote Sensing*, 17, 2029–2039.
- Lee, D. T. (1982). Medial axis transformation of a planar shape. *IEEE transactions on Pattern Analysis and Machine Intelligence*, 4, 363–369.
- Lee, D. S., Storey, J. C., Choate, M. J., & Hayes, R. W. (2004). Four years of Landsat-7 on-orbit geometric calibration and performance. *IEEE Transactions on Geoscience and Remote Sensing*, 42, 2786–2795.
- Lobell, D. B., Asner, G. P., Ortiz-Monasterio, J. V., & Benning, T. L. (2003). Remote sensing of regional crop production in the Yaqui Valley, Mexico: Estimates and uncertainties. *Agriculture, Ecosystems and Environment*, 94, 5–220.
- MacDonald, R. B., & Hall, F. G. (1980). Global crop forecasting. *Science*, 208, 670–679.
- Malladi, R., Sethian, J., & Vemuri, B. (1995). Shape modeling with front propagation: A level set approach. *IEEE transactions on Pattern Analysis and Machine Intelligence*, 17, 158–175.
- Markham, B.L., & Helder, D. L. (2012). Forty-year calibrated record of earth-reflected radiance from Landsat: A review. *Remote Sensing of Environment*, 122, 30–40.
- Markham, B.L., Storey, J. C., Williams, D. L., & Irons, J. R. (2004). Landsat sensor performance: History and current status. *IEEE Transactions on Geoscience and Remote Sensing*, 42, 2691–2694.
- Mason, D. C., Corr, D.G., Cross, A., Hogg, D. C., Petrou, M., Lawrence, D. H., et al. (1988). The use of digital map data in the segmentation and classification of remotely-sensed images. *International Journal of Geographical Information Science*, 2, 195–215.
- Mayer, H. (2008). Object extraction in photogrammetric computer vision. *ISPRS Journal of Photogrammetry and Remote Sensing*, 63, 213–222.
- Myint, S. W., Gober, P., Brazel, A., Grossman-Clarke, S., & Weng, Q. H. (2011). Per-pixel vs. object-based classification of urban land cover extraction using high spatial resolution imagery. *Remote Sensing of Environment*, 115, 1145–1161.
- Nickerson, C., Ebel, R., Borchers, A., & Carriazo, F. (2011). Major uses of land in the United States, 2007. EIB-89 U.S. Department of Agriculture, Economic Research Service (December 2011).
- Osher, S., & Sethian, J. A. (1988). Fronts propagating with curvature-dependent speed: Algorithms based on Hamilton-Jacobi formulations. *Journal of Computational Physics*, 79, 12–49.
- Ozdogan, M. (2010). The spatial distribution of crop types from MODIS data: Temporal unmixing using independent component analysis. *Remote Sensing of Environment*, 114, 1190–1204.

- Ozdogan, M., & Woodcock, C. E. (2006). Resolution dependent errors in remote sensing of cultivated areas. *Remote Sensing of Environment*, 103, 203–217.
- Ozesmi, S. L., & Bauer, M. E. (2002). Satellite remote sensing of wetlands. *Wetlands Ecology and Management*, 10, 381–402.
- Pan, Y., Li, L., Zhang, J., Liang, S., Zhu, X., & Sulla-Menashe, D. (2012). Winter wheat area estimation from MODIS-EVI time series data using the crop proportion phenology index. *Remote Sensing of Environment*, 119, 232–242.
- Pavlidis, T., & Liow, Y. T. (1990). Integrating region growing and edge detection. *IEEE Transactions on Pattern Analysis and Machine Intelligence*, 12, 225–233.
- Persello, C., & Bruzzone, L. (2010). A novel protocol for accuracy assessment in classification of very high resolution images. *IEEE Transactions on Geoscience and Remote Sensing*, 48, 1232–1244.
- Pitts, D. E., & Badhwar, G. (1980). Field size, length, and width distributions based on LACIE ground truth data. *Remote Sensing of Environment*, 10, 201–213.
- Pla, F. (1996). Recognition of partial circular shapes from segmented contours. *Computer Vision and Image Understanding*, 63, 334–343.
- Plourde, J.D., Pijanowski, B. C., & Pekin, B. K. (2013). Evidence for increased monoculture cropping in the Central United States. *Agriculture, Ecosystems & Environment*, 165, 50–59.
- Rao, N. R. (2008). Development of a crop-specific spectral library and discrimination of various agricultural crop varieties using hyperspectral imagery. *International Journal of Remote Sensing*, 29, 131–144.
- Roy, D. P. (2000). The impact of misregistration upon composited wide field of view satellite data and implications for change detection. *IEEE Transactions on Geoscience and Remote Sensing*, 38, 2017–2032.
- Roy, D. P., & Boschetti, L. (2009). Southern Africa validation of the MODIS, L3JRC and GLOBCARBON burned area products. *IEEE Transactions on Geoscience and Remote Sensing*, 47(4), 1032–1044.
- Roy, D. P., Ju, J., Kline, K., Scaramuzza, P. L., Kovalsky, V., Hansen, M., et al. (2010). Web-enabled Landsat Data (WELD): Landsat ETM+ composited mosaics of the conterminous United States. *Remote Sensing of Environment*, 114, 35–49.
- Roy, D. P., Qin, Y., Kovalsky, V., Vermote, E. F., Ju, J., Egorov, A., et al. (2014). Conterminous United States demonstration and characterization of MODIS-based Landsat ETM+ atmospheric correction. *Remote Sensing of Environment*, 140, 433–449.
- Rudel, T. K., Schneider, L., Uriarte, M., Turner, B.L., Defries, R., Lawrence, D., et al. (2009). Agricultural intensification and changes in cultivated areas, 1970–2005. *Proceedings of the National Academy of Sciences*, 106, 20675–20680.
- Rydberg, A., & Borgefors, G. (2001). Integrated method for boundary delineation of agricultural fields in multispectral satellite images. *IEEE Transactions on Geoscience and Remote Sensing*, 39, 2514–2519.
- Sakamoto, T., Wardlow, B.D., Gitelson, A. A., Verma, S. B., Suyker, A. E., & Arkebauer, T. J. (2010). A two-step filtering approach for detecting maize and soybean phenology with time-series MODIS data. *Remote Sensing of Environment*, 114, 2146–2159.
- Serra, J. (1988). *Image analysis and mathematical morphology, volume 2: Theoretical advances*. London Academic Press.
- Shackelford, K., & Davis, C. H. (2003). A combined fuzzy pixel-based and object-based approach for classification of high-resolution multispectral data over urban areas. *IEEE Transactions on Geoscience and Remote Sensing*, 41, 2354–2363.
- Smereka, M., & Dulęba, I. (2008). Circular object detection using modified Hough Transform. *International Journal of Applied Mathematics and Computer Science*, 18, 85–91.
- Ton, J., Sticklen, J., & Jain, A. K. (1991). Knowledge-based segmentation of Landsat images. *IEEE Transactions on Geoscience and Remote Sensing*, 29, 222–231.
- Tucker, C. J. (1979). Red and photographic infrared linear combinations for monitoring vegetation. *Remote Sensing of Environment*, 8, 127–150.
- Tucker, C. J., Elgin, J. H., Jr., McMurtrey, J. E., III, & Fan, C. J. (1979). Monitoring corn and soybean crop development with hand-held radiometer spectral data. *Remote Sensing of Environment*, 8, 237–248.
- USDA (2008). U.S. Department of Agriculture Food, Conservation, and Energy Act. http://www.drn.usda.gov/foia/2008FCEA_Section1619.pdf
- Wardlow, B.D., & Egbert, S. L. (2008). Large-area crop mapping using time-series MODIS 250 m NDVI data: An assessment for the U.S. Central Great Plains. *Remote Sensing of Environment*, 112, 1096–1116.
- White, M.A., de beurs, K. M., Didan, K., Inouye, D. W., Richardson, A.D., Jensen, O. P., et al. (2009). Intercomparison, interpretation, and assessment of spring phenology in North America estimated from remote sensing for 1982–2006. *Global Change Biology*, 15, 2335–2359.
- Zhu, Z., & Woodcock, C. E. (2012). Object-based cloud and cloud shadow detection in Landsat imagery. *Remote Sensing of Environment*, 118, 83–94.